The characteristics of bubbly shock waves in a cavitating axisymmetric venturi via time-resolved X-ray densitometry

Gawandalkar, U.U.; Poelma, C.

DOI
10.1017/jfm.2024.435

Publication date
2024

Document Version
Final published version

Published in
Journal of Fluid Mechanics

J. Fluid Mech. (2024), *vol*. 988, A34, doi:10.1017/jfm.2024.435

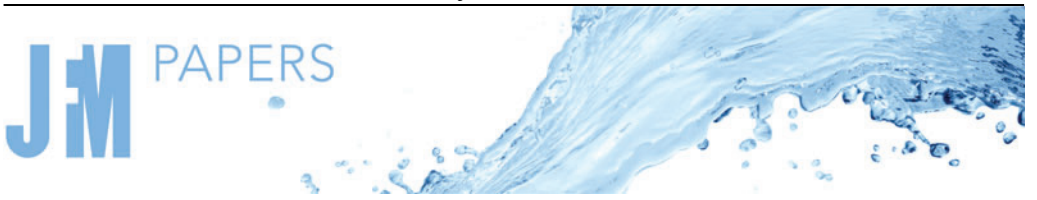

The characteristics of bubbly shock waves in a cavitating axisymmetric venturi via time-resolved X-ray densitometry

Udhav U. Gawandalkar[1],† **and Christian Poelma**[1]

[1]Process and Energy, Mechanical Engineering, Delft University of Technology, Leeghwaterstraat 39, 2628 CB Delft, The Netherlands

(Received 31 July 2023; revised 5 April 2024; accepted 26 April 2024)

The bubbly shock-driven partial cavitation in an axisymmetric venturi is studied with time-resolved two-dimensional X-ray densitometry. The bubbly shock waves are characterised using the vapour fraction and pressure changes across it, propagation velocity, and Mach number. The sharp changes in vapour fraction measured with X-ray densitometry, combined with high-frequency dynamic pressure measurements, reveal that the interaction of the pressure wave with the vapour cavity dictates the shedding dynamics. At the lowest cavitation number ($\sigma \sim 0.47$), the condensation shock front is the predominant shedding mechanism. However, as σ increases ($\sigma \sim 0.78$), we observe an upstream travelling pressure discontinuity that changes into a condensation shock as it approaches the venturi throat. This coincides with the increasing strength of the bubbly shock wave as it propagates upstream, manifested by the increasing velocity of the shock front and the pressure rise across it. Consequently, the Mach number of the shock front increases and surpasses the critical value 1, favouring condensation shocks. Further, at higher σ ($\sim$0.84–0.9), both the re-entrant jet and pressure wave can cause cavity detachment. However, at such σ, the pressure wave likely remains subsonic. Hence cavity condensation is not favoured readily. This leads to the re-entrant jet causing the cavity detachment at higher σ. The shock front is accelerated as it propagates upstream through the variable cross-section of the venturi. This enhances its strength, favouring cavity condensation and eventual shedding. These observations explain the existence of shock fronts in an axisymmetric venturi for a large range of σ.

Key words: cavitation, multiphase flow

† Email address for correspondence: u.u.gawandalkar@tudelft.nl

1. Introduction

Hydrodynamic cavitation can occur in a wide variety of flows, such as flow near ship propeller blades, throttle valves and fuel injectors (Blake & Gibson 1987). Partial cavitation is a commonly occurring form of cavitation, where attached vapour cavities are formed in the low-pressure regions. They get destabilised and are shed periodically or quasi-periodically, depending on the flow condition. The shed vapour then gets convected to a relatively high-pressure region, where it implodes (Brennen 1995). This inherent unsteadiness can lead to unwanted and detrimental effects such as noise, vibration, erosion wear, or even a catastrophic failure of the flow equipment. Hence understanding the fundamental physics of such flows is crucial. Specifically, it becomes imperative to understand the underlying vapour cavity destabilising mechanisms.

Classically, it was believed that the periodically generated re-entrant jet travelling below the vapour cavity is the sole mechanism responsible for cavity destabilisation and cloud cavitation (Knapp 1958; Kawanami *et al.* 1997; Callenaere *et al.* 2001). On the other hand, the watershed study of Reisman, Wang & Brennen (1998) and the subsequent studies of Arndt *et al.* (2000) and Leroux, Astolfi & Billard (2004) hypothesised an alternative cavity destabilising/shedding mechanism: it was proposed that a bubbly shock wave emanating from the coherent cloud collapse can dictate the cavity shedding dynamics. The recent experimental study of Ganesh, Makiharju & Ceccio (2016) and the supporting numerical studies (Gnanaskandan & Mahesh 2016*a*) demonstrated that indeed bubbly shock waves emanating from the collapse of a relatively large cavitation cloud play a crucial, if not dominant, role in the dynamics of cloud cavitation. Since then, this alternative shedding mechanism has been identified in various flow geometries (Jahangir, Hogendoorn & Poelma 2018; Brandao, Bhatt & Mahesh 2019; Trummler, Schmidt & Adams 2020). Further, the shedding mechanism is seen to change gradually from re-entrant jet to bubbly shock as the cavitation number (σ) decreases with a transition region, where both shedding mechanisms are seen to operate. The cavitation number expresses the intensity of the cavitation, as defined later. Using particle image velocimetry (PIV) applied to the near-wall flow, Gawandalkar & Poelma (2022) showed that re-entrant flow is present at the cavity closure region even at low σ. Further, it weakens severely at lower σ as the vapour cavity grows long enough such that it experiences a low adverse pressure gradient that drives the re-entrant jet. Interestingly, the numerical study of Budich, Schmidt & Adams (2018) proposed that cloud collapse is not a necessary condition for shock front formation. Rather, it was suggested that an adverse pressure gradient is a sufficient condition for shock formation. Alluding to this, Trummler *et al.* (2020) used large eddy simulations and proposed that the re-entrant jet gets converted into a condensation shock as it travels upstream. Recently, Zhang *et al.* (2022) proposed a third cavity destabilising mechanism due to the collapse-induced pressure wave. Zhang *et al.* (2022) observed that a collapse-induced pressure wave does not result in a vapour fraction discontinuity when it propagates through the vapour cavity, although it can arrest its growth. Hence there is no consensus on the phenomenological description of cavity destabilisation, especially the role of cloud collapse on the overall cavity dynamics. Additionally, the flow conditions favouring the respective shedding mechanism and the cause of transition of the shedding mechanism from re-entrant jet to bubbly shock wave still remain open questions. It is worthwhile to note that the disparate shedding mechanisms give rise to different cavitation dynamics, such as shedding frequency and maximum pressure pulse, which can influence the degree of unsteadiness and wear.

Cavitating flows are generally a highly turbulent, bubbly mixture. Further, the morphology of the vapour cavity is such that it is a nearly homogeneous mixture of liquid

and vapour. Even a modest vapour fraction ($\sim$0.05) can significantly reduce the speed of sound in the bubbly mixture, making the fluid locally supersonic at a velocity of the order of the bulk flow velocity (Ganesh *et al.* 2016; Bhatt & Mahesh 2020). As cavitation develops with decreasing σ, the vapour fraction of the flow is expected to be significantly higher. This makes bubbly flows highly compressible and susceptible to condensation shocks (Brennen 1995; Prosperetti 2015). It has been demonstrated that the local Mach number (Ma) of the propagating bubbly shock front in a developed cavitation flow could be as high as 4 (Brandao *et al.* 2019). In order to assess the effect of compressibility in cavitating flows, the quantification of vapour fraction and the pressure of the bubbly mixture becomes vital. Moreover, cloud cavitation, i.e. the implosion of the shed cloud, will inevitably give rise to a pressure wave. The strength of this pressure wave and its interaction with the attached vapour cavity dictate the cavity shedding dynamics. In order to observe and study this interaction, it is also necessary to quantify the strength of the pressure wave. More importantly, it is imperative to see through the occluding vapour cavity. However, the bubbly–frothy nature of the flow presents a significant challenge to make a meaningful experimental observation. Naturally, the efficacy of light-based measurement techniques (such as shadowgraphy and PIV) is limited due to the lack of optical access induced by the opacity of the vapour cavity. Thus non-optical measurement techniques such as X-ray densitometry or magnetic resonance imaging are favoured (Poelma 2020). Furthermore, the cloud shedding and collapse dynamics occur at small time scales. Thus whole-field, time-resolved measurements of vapour fractions are essential to gain insights into cavitating flow physics.

To this end, X-ray densitometry is emerging as a promising qualitative and quantitative measurement technique for studying cavitation dynamics. The ability of X-rays to penetrate through the liquid–vapour interface can circumvent the issues of optical artefacts manifested by refraction, diffraction and multiple scatterings (Aliseda & Heindel 2021). Further, absorption-based X-ray imaging can provide quantitative information on the composition of two-phase mixtures. Stutz & Legoupil (2003) and Coutier-Delgosha *et al.* (2006) carried out vapour fraction measurements, with X-ray densitometry in a two-dimensional venturi and two-dimensional hydrofoil, respectively, to investigate the two-phase morphology and the vapour fraction within the cavity. Further, Jahangir *et al.* (2019) studied cavitation in an axisymmetric venturi using time-averaged X-ray densitometry followed by computed tomography, akin to Mitroglou *et al.* (2016). Similarly, Zhang *et al.* (2020) and Karathanassis *et al.* (2021) used synchrotron X-ray densitometry to study time-averaged vapour fractions to generate insights into cloud cavitation in a micro-venturi and a cylindrical orifice, respectively. These time-averaged measurements provide only a limited insight into the highly unsteady partial cavitation phenomena. The copious amount of literature originating from the group at the University of Michigan (Ann Arbor, USA) with high-speed X-ray densitometry (Mäkiharju *et al.* 2013) has generated invaluable acumen into the physics of partial cavitation. Although their measurement system has a sufficiently high spatial resolution, the temporal resolution is insufficient to capture the entire shedding dynamics.

Furthermore, it has been shown that cavitation dynamics can be unique for each canonical flow geometry, such as wedges (Ganesh *et al.* 2016), hydrofoils (Wu, Ganesh & Ceccio 2019), backward-facing steps (Bhatt, Ganesh & Ceccio 2021) and bluff bodies (Wu *et al.* 2021). It should be noted that these studies are limited to external flows. The axisymmetric venturi, on the other hand, has a significant pressure gradient induced by virtue of geometric confinement, i.e. walls (blockage). For instance, the area-based blockage (contraction ratio) in the aforementioned external flows is limited

to 3 (Ganesh *et al.* 2016) and 1.15 (Bhatt *et al.* 2021). However, for the current geometry, the area-based blockage is ∼9, which is substantially higher. Evidently, less attention is dedicated in the literature to characterising the dynamics and kinematics of the condensation shock front that dictates the cavity shedding in internal flows, despite the significant industrial relevance, such as venturis and throttle valves. Moreover, Jahangir *et al.* (2018) reported that the bubbly shock front underwent severe acceleration as it approached the throat. Therefore, the kinematics of the condensation shock front and its influence on the shedding dynamics is worth exploring.

In this study, we aim to clarify the role of the pressure wave emanating from the cloud implosion in periodic cloud cavitation at different flow conditions (σ). We employ an axisymmetric venturi as the flow geometry, as it remains less explored in the literature. Further, it allows us to build upon the insights gained from previous studies of Jahangir *et al.* (2018) and Gawandalkar & Poelma (2022). Time-resolved (3.6–6 kHz) X-ray densitometry is employed in conjunction with time-synchronised, high-frequency (100 kHz) dynamic pressure measurements and high-speed shadowgraphy to (i) track the propagating pressure discontinuity for the first time, (ii) visualise the interaction of the bubbly shock waves with the growing vapour cavity, and (iii) decipher the role of this interaction on the cavitation dynamics. This is done by quantifying characteristics of the pressure wave propagating in the low vapour fraction liquid and the bubbly shock front that is formed upon the impingement of the pressure wave on the growing cavity. The bubbly shock fronts are characterised by the vapour fraction and the pressure rise across the shock front along with the shock front velocity. The pressure rise across the front and its Mach number are used as proxies for the strength of the condensation front. The decreasing strength of the bubbly shock front (with increasing σ) is used to corroborate the observed cavitation dynamics at different σ. Our investigation shows that the kinematics – i.e. the acceleration of the condensation shock front – can play a significant role in dictating the cavity shedding dynamics in a high-blockage axisymmetric venturi. Based on this, we propose a modified phenomenological description of cavity shedding dynamics. A simple model can be constructed, which agrees with our experimental observations. Supersonic shock fronts are hypothesised to be readily favoured in such converging geometries, resulting in the destabilisation of vapour cavities via condensation.

This paper is organised as follows. A description of the experimental set-up, measurement technique and data processing approach is detailed in § 2. The results are reported in § 3, where the vapour cavity topology, such as shape and vapour fractions, is presented. Additionally, we discuss the time-resolved cavity dynamics at different cavitation numbers. The observed shedding dynamics are corroborated by quantifying the characteristics of the bubbly shock waves. Moreover, we shed light on the kinematics of the condensation shock front and its interplay with the shedding dynamics, supported by a simple model. Finally, the phenomenological description of cavity shedding dynamics in an axisymmetric venturi is summarised in § 4.

2. Experimental set-up and methodology

2.1. *Flow facility*

The experiments were performed in a cavitation loop, described in detail in Jahangir *et al.* (2018). Tap water is used as a working fluid, which was deionised, filtered and de-gassified for several hours before performing experiments. The flow is driven by a centrifugal pump, while the volumetric flow rate is measured with a magnetic inductive flow meter (KROHNE). The flow loop consists of Plexiglas pipe sections with inner

No.	P_d (kPa)	P_v (kPa)	U_t (m s^{-1})	Re_t	σ
1	59.9	3.83	11.15	1.86×10^5	0.90
2	56.36	3.42	11.22	1.87×10^5	0.84
3	56.17	3.59	11.59	1.93×10^5	0.78
4	59.33	4.01	12.91	2.15×10^5	0.67
5	59.39	4.22	13.49	2.25×10^5	0.61
6	56.38	3.86	13.54	2.25×10^5	0.57
7	44.95	3.67	13.38	2.23×10^5	0.47
8	36.26	4.56	12.80	2.13×10^5	0.39

Table 1. The flow parameters at different cavitation numbers (σ).

diameter $D = 50$ mm. Cavitation is realised at the throat of the axisymmetric venturi with divergence angle 8°, which is installed $50D$ downstream of the last elbow. This acts as a flow development length, such that the incoming flow is fully developed turbulent pipe flow. The venturi has throat diameter $D_t = 16.67$ mm, leading to area-based contraction ratio 9. The flow loop allows independent control of the flow rate and the global static pressure via a vacuum pump. The intensity of cavitation is dictated by the cavitation number (σ), defined as $\sigma = (P_d - P_v)/(\frac{1}{2}\rho U_t{}^2)$. Here, P_d is the far-downstream pressure, P_v is the vapour pressure, and U_t is the throat velocity, where P_v and the kinematic viscosity of the working fluid are determined using the measured temperature of the liquid during each run. In the current work, σ was varied between 0.39 and 0.90 by varying the global static pressure and U_t independently (see table 1 for detailed flow conditions). For consistency and comparison, the reproducibility of the flow was established by comparing global cavitation dynamics ($St_t = fD_t/U_t$ as a function of σ, where $f = 1/T$ is the cavity shedding frequency, and T is the shedding time period) with the previous studies.

2.2. *X-ray densitometry*

The time-resolved X-ray densitometry measurements were performed at the High-Speed X-ray (HSX) facility of TNO Ypenburg – The Hague, The Netherlands, shown in figure 1(*a*). The X-ray imaging facility consists of a Varian Medical Systems tube X-ray source capable of producing 150 kV at 80 kW. The anode insert is made of rhenium-tungsten molybdenum and produces a fan-beam of a maximum 12° cone angle. The source is coupled with a scintillator plate and image intensifier, wherein the attenuated X-ray (electrons) are converted into visible light. This is then imaged with a high-speed camera (Photron, FASTCAM NOVA S-12, 12 000 fps at 1 megapixel) placed perpendicular to the scintillator plate as shown in figure 1(*b*). The scintillator plate and the image intensifier are made of the fastest Phosphor (P46), which has decay time approximately 20 μs. This ensures minimum 'ghosting' in the time series of X-ray images, allowing higher temporal resolution. It is crucial to note that the obtained X-ray images (radiographs) are z-averaged, i.e. along the X-ray beam direction. The density measurements via X-ray are based on the attenuation of the X-ray intensity by different materials through which it passes, governed by the Beer–Lambert law. Thus by recording the incident intensity (I_0) and the intensity after passing through the bubbly flow (I), the

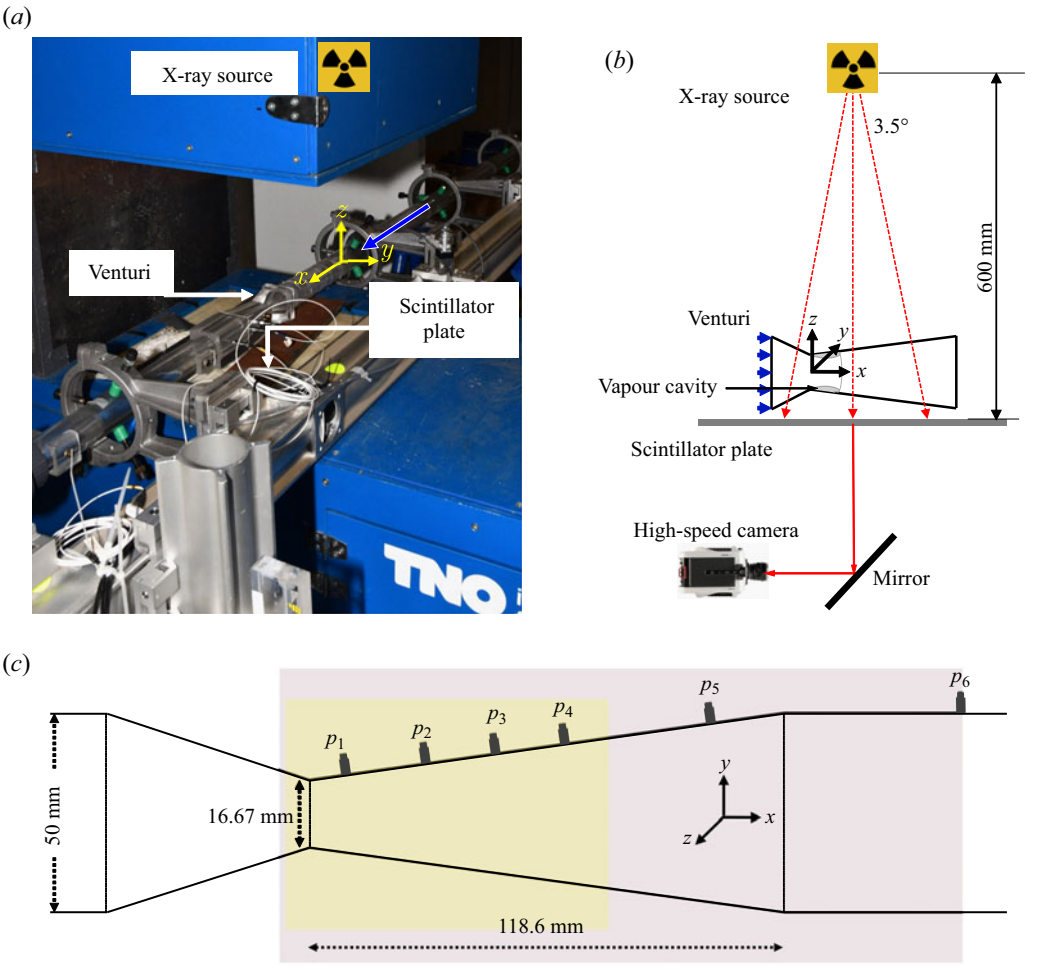

Figure 1. (*a*) High speed X-ray (HSX) measurement imaging system at TNO-Ypenburg with the cavitation loop; the blue arrow shows the direction of bulk flow. (*b*) A schematic of the measurement system. (*c*) Schematic showing the dimensions of the venturi, the position of the pressure ports, and the field of view of the X-ray densitometry (yellow) and high-speed imaging (grey).

mass density of fluid integrated along the X-ray beam path can be obtained as

$$\frac{I}{I_0} = \exp\left(-\sum_{i=1}^{N} \mu_i \rho_i x_i\right). \tag{2.1}$$

Here, I is the received intensity, I_0 is the incident intensity, μ_i is the medium attenuation coefficient, ρ_i is the medium mass density, and x_i is the path length through a medium. The summation accounts for multiple mediums such as Plexiglas, liquid and vapour. The X-ray source is at a distance approximately 590 mm from the test section. The beam is incident on the test section in the x–z plane. The axisymmetric venturi test section is modified such that the amount of Plexiglas that is encountered by the X-ray beam is minimal, while maintaining structural integrity. This ensures low X-ray baseline attenuation to augment the signal to noise ratio in the radiographs. The field of view (FOV) spans 70×50 mm^2, wherein the centre of the beam approximately coincides with the centre of the FOV (see

the yellow region in figure 1*c*). Hence the maximum angles subtended by the beam in the x-direction and y-direction are 3.4° and 2.4°, respectively (see figure 1*b*). Thus it can be assumed that the X-ray beam is nearly parallel as it passes through the region of interest. In the current experimental campaign, the X-ray source is operated at amperage 710 mA and voltage 40 kV. This allowed enough separation in the X-ray image counts (contrast) to quantify the expected densities (0.8–1000 kg m^{-3}) in this geometry. With these settings, the X-ray source had a maximum run time of 0.63 s to avoid overheating of the anode. This enabled us to capture at least 32 shedding cycles for the slowest cavity shedding. The images are acquired at frequency 18 000 Hz.

2.3. *High-speed imaging*

The cavity shedding dynamics are also visualised using conventional high-speed shadowgraphy to supplement the time-resolved X-ray densitometry. The FOV is centred along the venturi axis and spans 189 × 64 mm^2 in the x–z plane, which is orthogonal to and larger than the FOV used in X-ray imaging (see the grey region in figure 1*c*). It is back-illuminated with a continuous white LED source. A high-speed CMOS camera (Photron Fastcam APX RS) equipped with an objective lens of 105 mm and aperture f/7.2 ensures sufficient contrast between the liquid and vapour phases. The images are acquired at a rate of 18 000 Hz with exposure time 1/18 000 s.

2.4. *Pressure measurements*

The high-speed X-ray densitometry and shadowgraphy are complemented with high-frequency dynamic pressure measurements at various axial locations (p_1 to p_6; see figure 1*c*). The pressure port locations (p_1 to p_6) measured from the venturi throat are 0.6, 1.45, 2.5, 3.6, 5.9, 10.2 times D_t, respectively. We employ several flush-mounted PCB 102 sensors with sensitivity 0.15 mV kPa^{-1} and rise time <1 µs to pick up the fluctuations in local pressures at the specified axial locations (see again figure 1*c*). The pressure transducer has a nearly flat transfer function up to the sampling frequency 300 kHz. Thus pressure signals are reliably acquired at 100 kHz. The dynamic pressure acquisition is time-synchronised with the X-ray imaging using an external signal generator (KEYSIGHT 33210A). This is done with the aim of quantifying the pressure peak brought about by the cavitation cloud implosion and pressure rise due to the propagating bubbly shock, through both the liquid and the attached vapour cavity. The pressure rise brought about by the condensation shock front in the attached cavity is measured at locations p_1 to p_3. The pressure peak due to the cloud implosion is measured at p_4 to p_6. Pressure transducers at multiple locations are used because (i) the expected cloud collapse region is a function of σ, and (ii) the high-frequency response of multiple pressure sensors at a fixed distance allows us to track the propagating pressure wave and thus estimate its propagation velocity in the low vapour fraction liquid. The unsteady static pressure in the cavity is measured at a fixed axial location (p_1) in a separate set of experiments using a flush-mounted IPSL series piezo-resistive silicon sensor with accuracy 0.25 % of its full scale (0–100 kPa) and response time ∼1.5 ms. The static pressure data are time-synchronised with high-speed imaging to omit the pressure data segments where the cavity does not cover the static pressure transducer.

2.5. *Projected vapour fraction estimation*

The raw X-ray images are enhanced to eliminate vertical stripes due to the electronic noise of the camera sensor. This is done using Fourier-based stripe filtering (Münch *et al.* 2009), followed by a median filtering with kernel size 5×5 pixels. This resulted in a maximum loss of 1 % in the energy (I^2) in the image. Further, a spatial mean filter of the same kernel size is applied to eliminate high-frequency noise. The image intensity of the bubbly mixture (I_m) is converted to a vapour fraction (α) using a two-point calibration approach as

$$\alpha = \frac{\log \dfrac{I_m}{I_w}}{\log \dfrac{I_a}{I_w}}. \tag{2.2}$$

This is based on assumptions that (i) the flow is strictly two-phase (water and vapour), i.e. the mixture density (ρ_m) can be expressed as $\rho_m = \alpha\rho_a + (1-\alpha)\rho_w$, where w and a are subscripts for water and air, respectively, (ii) the X-ray source is monochromatic (single energy), and (iii) the X-rays are nearly parallel. Further, a two-point calibration approach is deemed sufficient as also shown by Jahangir *et al.* (2019). The X-ray images of the venturi fully filled with water (I_w) and venturi fully empty/full air (I_a) were used for the calibration process. Note that air is used as a proxy for water vapour as their densities are comparable and almost three orders of magnitude lower than that of water. Further, a metal calibration grid is used for geometric calibration. Thus the projected vapour fractions are resolved with spatial resolution 0.45 mm ($0.027D_t$) and temporal resolution 1/3600 s (averaging over five frames) to 1/6000 s (averaging over three frames), depending on the cavitation number (σ). The cavitation dynamics is faster at higher σ, hence for these cases, we evaluate vapour fractions at a higher temporal resolution to capture essential flow dynamics. Furthermore, the signal-to-noise ratio in X-ray radiographs reduced for higher σ due to low vapour fractions in the flow. Hence the vapour fraction could not be measured reliably for $\sigma > 0.90$. This also precludes pressure wave characterisation at such σ. In order to make a rough estimate of the uncertainty level in vapour fraction measured via the current X-ray densitometry system, we examined the measured vapour fraction upstream of the venturi throat. This region contains pure liquid for which the vapour fraction ought to be 0. The measured instantaneous vapour fraction upstream is <0.05.

2.6. *Planar vapour fraction estimation*

In the axisymmetric venturi, the vapour formation is localised in the near-wall region due to the pressure field. Consequently, the z-projected X-ray images estimate vapour fraction close to the wall with good accuracy; however, they will overestimate vapour fractions in the core of the venturi. Thus the time-averaged ($\overline{\alpha(x, y)}$) and the phase-averaged ($\langle\alpha(x, y, t/T)\rangle$) projected vapour fractions are back-projected using filtered back projection (FBP) via the ASTRA toolbox (van Aarle *et al.* 2016) to yield planar vapour fractions. This is commonly referred to as computed tomography (CT). A similar approach was used by Mitroglou *et al.* (2016) and Jahangir *et al.* (2019) to estimate time-averaged void fractions. However, due to the high temporal resolution in this study, we extend their approach to phase averages to resolve vapour fractions in a shedding cycle. The demonstrated periodicity in the cavitation dynamics allows us to perform phase-averaging similar to Gawandalkar & Poelma (2022). It is, however, imperative to realise that CT does not

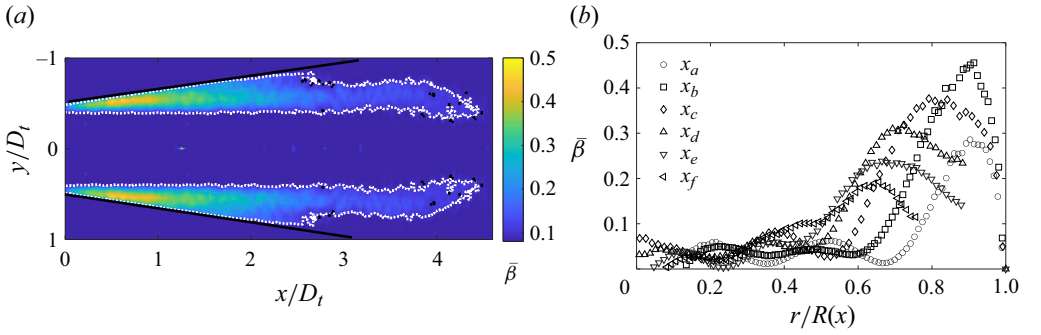

Figure 2. (*a*) Time-averaged back-projected planar vapour fraction field ($\bar{\beta}$). The white dotted outline indicates the vapour–liquid interface ($\bar{\beta} = 0.1$), while the black solid lines indicate the venturi wall. (*b*) Profiles of $\bar{\beta}$ at different axial locations (x_a to x_f: 0.12, 0.55, 1.1, 1.7, 2.2, 2.8 times D_t) in the venturi for $\sigma = 0.47$, where $R(x)$ is the local venturi radius.

provide any additional information in the present study as the imaging is limited to a single camera view. The aim of CT is thus to estimate the planar (x–y) vapour fraction fields (β) to provide experimental data for the validation of numerical models. This approach is subject to assumptions, i.e. (i) the X-rays passing through the attached cavity are near-parallel, and (ii) the attached cavity is axisymmetric in an averaged sense (time and phase). The CT reconstructions are performed on the z-projected averaged X-ray images (time and phase), which serve as an input to the FBP algorithm, while attenuation coefficients (μ_m) are generated as an output. Further, μ_m values are converted into β using the two-point calibration:

$$\beta = \frac{\mu^m - \mu^w}{\mu^a - \mu^w}. \tag{2.3}$$

The two reference points are the attenuation due to pure liquid (μ^w for $\beta = 0$) and pure vapour (μ^a for $\beta = 1$). This yields vapour fractions in a y–z plane, as detailed extensively in Jahangir *et al.* (2019). Further, this process is repeated for each axial location (x), and reconstructed y–z planes are stacked along the central axis of the venturi (x-axis). Finally, planar vapour fraction fields $\overline{\beta(x, y)}$ are extracted from the reconstructed three-dimensional vapour fraction fields at the centre plane. Similarly, phase-averaged planar void fractions ($\langle\beta(x, y, t/T)\rangle$) are also obtained.

3. Results

3.1. *Vapour fractions fields*

The time-averaged planar vapour fraction field ($\overline{\beta(x, y)}$), along with the radial profiles of $\overline{\beta(x, y)}$ for the lowest cavitation number ($\sigma = 0.47$), are shown in figures 2(*a*) and 2(*b*), respectively. It can be seen that $\overline{\beta(x, y)}$ achieves a maximum value 0.43 near the wall (close to the throat), while the vapour fraction is 0.05 in the core of the venturi, a value comparable to the measurement uncertainty. The time-averaged vapour fraction gradually reduces away from the throat as the vapour cloud is convected downstream. This is consistent with the previous observations of Jahangir *et al.* (2019), who measured time-averaged vapour fractions at $\sigma = 0.40$. Further, the instantaneous vapour fraction in a cycle (or a phase) can be as high as 0.68 at the same flow conditions; see figure 3. In the same figure, it can be seen that the maximum vapour fraction in a cycle is significantly

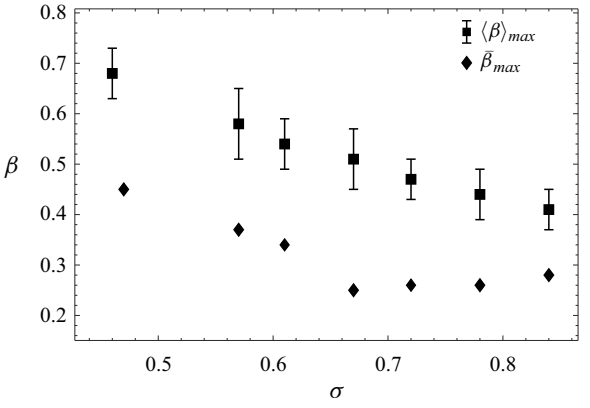

Figure 3. The phase-averaged maximum vapour fraction in a shedding cycle ($\langle\beta\rangle_{max}$) and the maximum time-averaged vapour fraction ($\bar{\beta}_{max}$), at different cavitation numbers (σ).

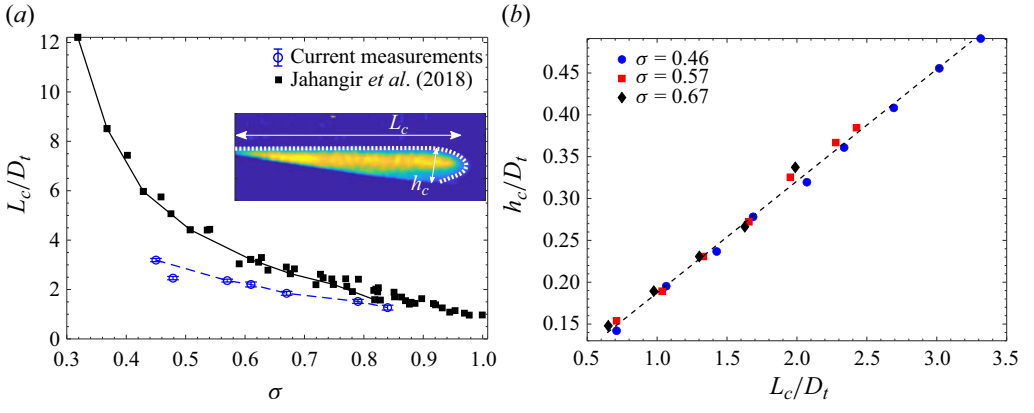

Figure 4. (*a*) Maximum cavity length (L_c) normalised with the throat diameter (D_t) as a function of the cavitation number (σ). Square markers show shadowgraphy measurements of Jahangir *et al.* (2018), while circles show current X-ray densitometry measurements. The white dotted outline in the inset shows the isocontour of $\beta = 0.1$, demarcating the cavity interface. (*b*) Maximum cavity thickness (h_c) normalised with D_t for different cavity lengths and σ.

higher than the maximum time-averaged vapour fraction. This is attributed to the temporal averaging of vapour fractions due to the periodic growth and collapse of the cavity. Further, the maximum vapour fraction decreases with increasing σ. This shows the necessity of time-resolved vapour fraction fields in such flows.

3.2. *Vapour cavity topology*

The phase-averaged planar vapour fractions $\langle\beta(x, y, t/T)\rangle$ also allow us to quantify the shape and size of the attached vapour cavity in a venturi. The Froude number ($Fr_{L_c} = U_t/\sqrt{gL_c}$) defined on the cavity length is $\gtrsim$20. Hence the effect of gravity on the cavity shape can be expected to be negligible. Further, the Weber number ($We_{L_c} = \rho U_t^2 L_c/\gamma$) is $O(10^4)$, so the effects of inertia dominate the surface tension (γ) effects. The isocontour of $\beta = 0.1$ is used to demarcate the boundary of the cavity; see the inset in figure 4(*a*). Since the attached vapour cavity grows in a shedding cycle, the maximum cavity length

(L_c) and maximum cavity height (h_c) are used to describe the topology of the attached cavity. The maximum cavity length for different σ is shown in figure 4(*a*). It can be seen that L_c/D_t measured by X-ray densitometry is systematically shorter than the results from shadowgraphy (Jahangir *et al.* 2018), with a deviation up to 50 % at $\sigma = 0.47$. This observation is not sensitive to our chosen threshold $\beta = 0.1$ to demarcate the cavity: L_c estimated with threshold $\beta = 0.05$ is about 4 pixels ($0.02D_t$) higher than with threshold $\beta = 0.1$. Also, L_c remains unaltered with an increase of threshold β from 0.1 to 0.15. The observed deviation could be attributed to the difficulty in defining the vapour content (vapour fractions) and thus cavity in shadowgraphs (Dash, Jahangir & Poelma 2018). The vapour bubbles detached from the cavity may appear to be a part of it in shadowgraphs, overestimating cavity lengths. The maximum height of the attached cavity (h_c) is also quantified (see figure 4*b*). It is observed that h_c increases monotonically with the cavity length. Further, cavity height scales directly with the cavity length, irrespective of the cavitation number.

3.3. *Vapour shedding dynamics*

The time-synchronised X-ray imaging with dynamic pressure (dp) measurements allows us to visualise the shedding dynamics and ascertain the role of a pressure wave in the shedding cycle at different cavitation numbers (σ). The instantaneous projected vapour fractions (α) are used to visualise the cavity dynamics. The colour indicates the vapour fraction: blue for a completely liquid phase, and yellow for a higher vapour content. Further, the cavity front evolution in a shedding cycle is studied with a space–time (x–t) plot of α. The fixed axial locations of the pressure transducers make dp measurement at the exact location of each cloud collapse cumbersome. Thus the dp measurement closest to each cloud collapse location is used to measure the cloud implosion pressure peak. This peak arrives at the transducer with a minor delay, as discussed in the next paragraph. A single representative shedding cycle will be shown for $\sigma = 0.47$, 0.78 and 0.84 in the following discussion.

The cavity dynamics at $\sigma = 0.47$ is illustrated in figure 5. The cavity is seen to grow from figure 5(*a*) to figure 5(*c*). As the cavity grows, there is a continuous re-entrant flow beneath the cavity at the closure region, as shown in figures 5(*b*) and 5(*c*). This is inferred from a fairly low vapour fraction close to the venturi wall ($\alpha \sim 0.2$) in comparison to the vapour cavity ($\alpha \sim 0.7$). The presence of a re-entrant jet for the considered range of σ was also observed directly by Gawandalkar & Poelma (2022) with near-wall velocimetry in the same flow geometry. At the instance marked by *d* in figure 5(*j*), the imploding cavitation cloud from the previous shedding cycle gives rise to a pressure wave, evident from a strong pressure peak in dp at p_6. The cloud collapse appears to have been coherent, as is evident from a single sharp peak of 340 kPa for a very short duration. The cloud collapse itself could not be visualised in the X-ray images at this σ, as the collapse is expected to occur at $x \sim 9D_t$, as observed in previous high-speed shadowgraphy (Jahangir *et al.* 2018). Note that the structure labelled 'Shed cloud' in figure 5(*e*) will result in a pressure peak in the next cycle. The pressure wave emanating from the collapse propagates through the low vapour fraction liquid: the high-frequency pressure transducers at p_5 and p_6 pick up the pressure wave propagating at velocity $u_{pw} \sim 450$ m s^{-1}. This is estimated using the time delay between the peaks and the distance between the transducers. There is a small time delay between the cloud implosion and the pressure wave reaching the pressure transducer (∼0.04 ms, estimated using u_{pw} and transducer locations). Additionally, there is a time delay (∼0.24 ms) between the cloud collapse and the impingement (see next paragraph)

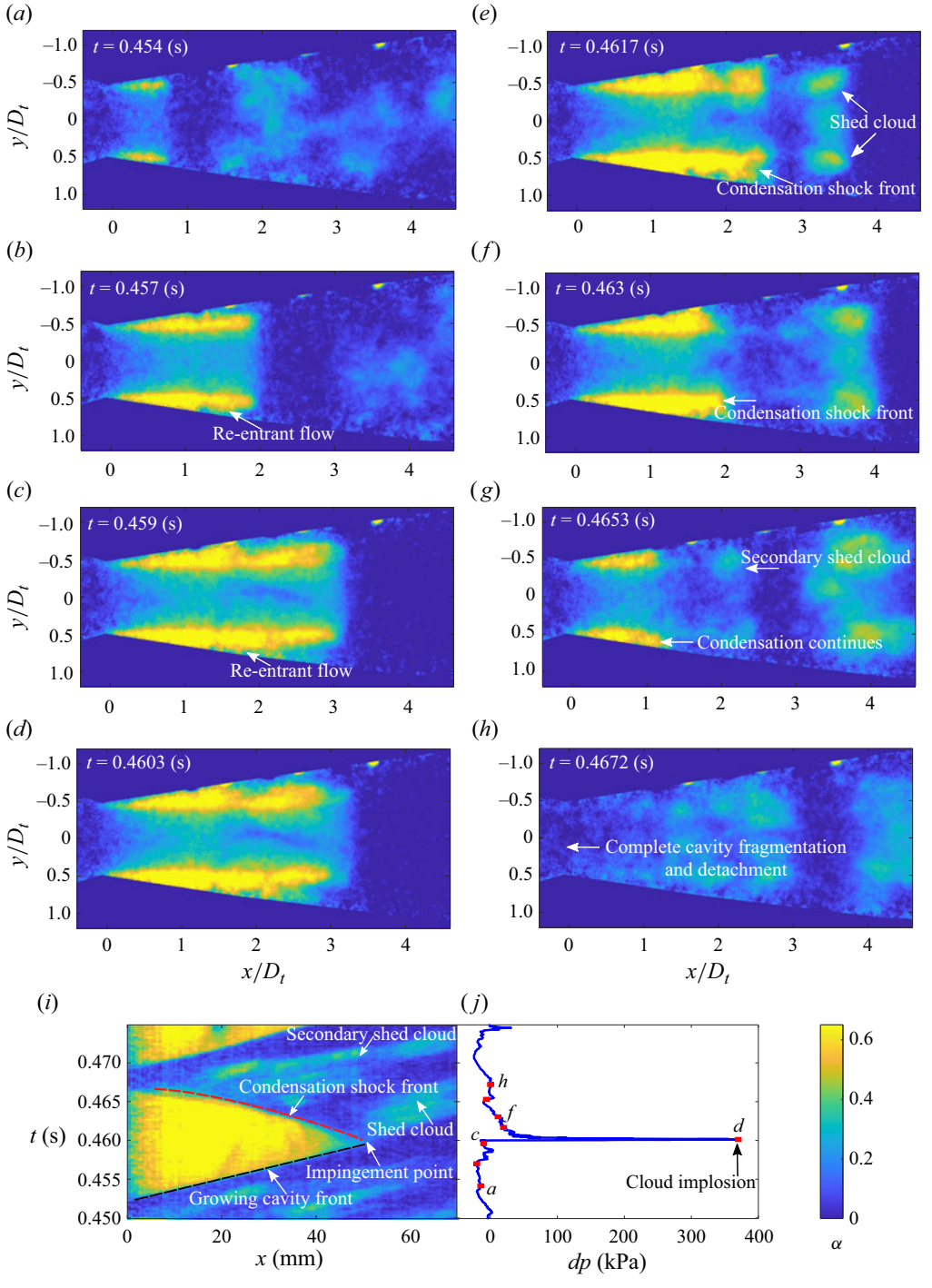

Figure 5. (*a–h*) A single shedding cycle at $\sigma = 0.47$. (*i*) The x–t evolution of the vapour fraction for this shedding cycle. (*j*) The time trace of the dynamic pressure recorded simultaneously at p_6. The bulk flow is from left to right. The colour indicates the z-projected vapour fractions.

on the cavity due to the finite distance between the cloud implosion and the impingement point. However, these time delays are negligible in comparison to the cavity shedding time period $T = 17.4$ ms, due to the much higher speed of the shock front in the low vapour fraction region compared to its value in the attached vapour cavity. For all intents and purposes, the x–t diagram and pressure signals can thus be considered to be synchronous, with no time delay between cloud collapse and impingement.

The upstream travelling pressure wave impinges on the attached cavity and arrests the cavity growth. Here, impingement is defined as the first point of interaction between the pressure wave and the attached cavity. The impingement leads to a maximum cavity length, referred to as L_c. The 'impingement point' can be seen in the x–t evolution of the cavity front in figure 5(*i*), where the growing cavity front is shown by a black dashed line, while the retracting cavity front is shown by a red dashed curve. Due to this impingement, a large part of the cavity gets shed (see figure 5*e*) and is then convected downstream with the bulk flow, where it will implode. After impinging, the upstream-travelling pressure wave immediately starts condensing the attached cavity. The condensation shock front is seen to travel upstream through the cavity, destabilising the attached cavity. This process is more clear in supplementary movie 1 available at https://doi.org/10.1017/jfm.2024.435. The shock front is also evident in the x–t diagram as shown in figure 5(*i*): it is shown by a red dashed curve and is characterised by a sharp decrease in vapour fraction across it. The inverse of the slope of the condensation shock front in the x–t plot is the shock front velocity.

It can be observed that the shock front accelerates significantly as it approaches the throat, as is evident from the changing slope of the shock front. This will be addressed in § 3.7. Further, some amount of vapour remains after the shock front has passed over the cavity and condensed it. This leads to low vapour fraction streaks in the x–t plot and is also indicated by 'Secondary shed cloud' in figure 5(*g*). This is suspected to be a result of the interaction of the bubbly shock wave with the attached cavity, which is essentially composed of coalesced vapour bubbles. The condensation shock front travels upstream and reaches the throat, resulting in complete cavity fragmentation and destabilisation. This is in line with the previous observations of Jahangir *et al.* (2018), Ganesh *et al.* (2016) and Budich *et al.* (2018) at low σ. This is followed by a brief period where the venturi throat is left 'cavitation-less'. Meanwhile, the shed cloud is convecting downstream. This completes a shedding cycle until a new cavity starts growing at the throat as described above.

It is worthwhile to note that in a few (three in forty) shedding cycles at $\sigma = 0.47$, multiple bubbly shock waves are seen to travel through the growing cavity (see figure 6), exhibiting multi-step cavity shedding modes. Interestingly, the implosion of the secondary shed cloud (from the previous cycle, shown in figure 6*a*) produces a weaker pressure wave ($dp \sim 30$ kPa, 'Collapse-1' in figure 6*k*). This gives rise to an upstream-travelling bubbly shock wave as indicated by 'CSF-1' (see the yellow arrow in figure 6). This is inferred from collapse-1 coinciding in time with the emergence of CSF-1 in figure 6(*j*). However, the rate of vaporisation at the throat is expected to be high, dictated by the pressure at the throat. Thus the cavity continues to grow to assume its maximum length (L_c). During this time, the bubbly shock wave (CSF-1) appears frozen for a while before it moves upstream very slowly, by the yellow arrow in figures 6(*c*)–6(*e*). The rate of vapour production near the throat is likely sufficiently high to oppose the shock front propagation. This is followed by a stronger cloud implosion ($dp \sim 260$ kPa, 'Collapse-2') producing a 'CSF-2' (see the red arrow in figure 6) that ultimately destabilises the cavity similar to the shedding cycle shown in figure 5. Furthermore, it is clear from the x–t plot (figure 6*j*) that the initial

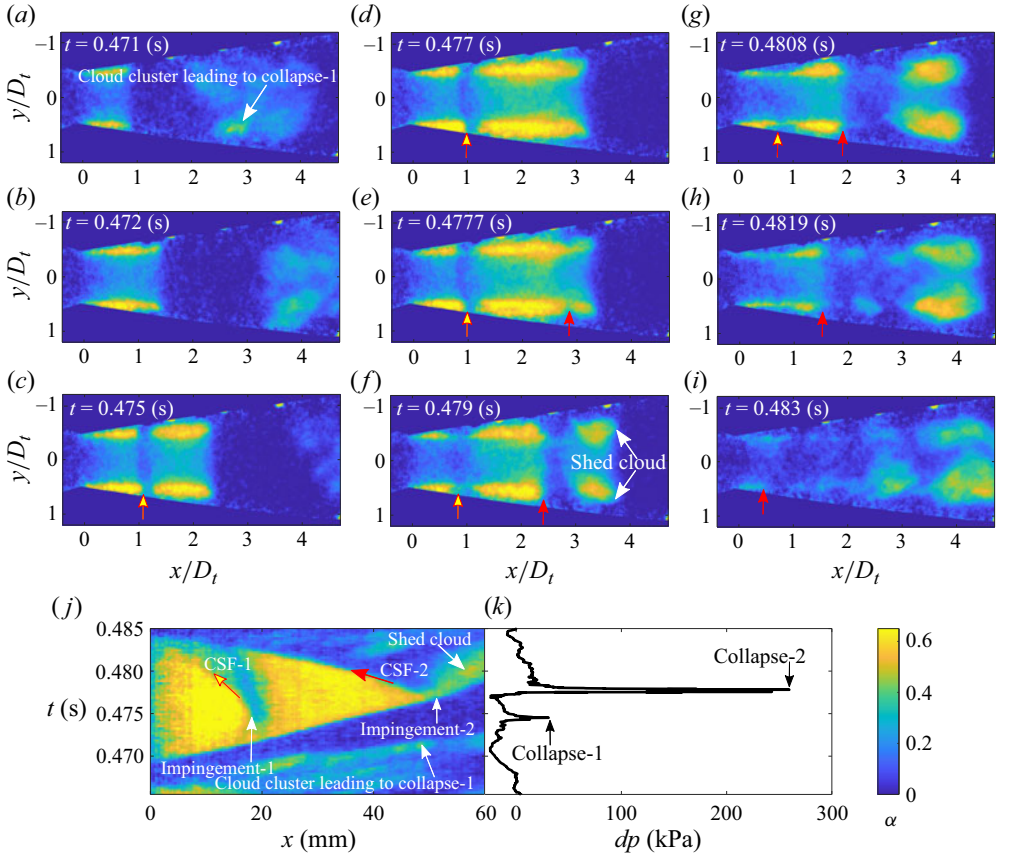

Figure 6. (*a–i*) A shedding cycle at $\sigma = 0.47$, showing multiple condensation shock fronts (CSF) in one cycle. (*j*) The *x–t* evolution of the cavity front. (*k*) The *dp* time trace recorded simultaneously at station p_6. The arrows show propagating condensation shock fronts: CSF-1 is marked by a yellow arrow with a red outline, while CSF-2 is marked by a full red arrow.

velocity of 'CSF-1' (-2.2 m s^{-1}) is substantially lower than that of 'CSF-2' (-6.4 m s^{-1}). Consequently, an earlier smaller cloud implosion does not have any consequence for the global shedding dynamics. Instead, the larger cloud implosion dictates the cloud shedding frequency.

Similarly, in a limited number of shedding cycles (two in forty), it is observed that the cavity undergoes asymmetric cavity detachment. It is seen that the upper (figure 7*a*) and lower (figure 7*b*) parts of the cavity show different growth and shedding behaviour. It is seen that the cavity starts condensing due to CSF-1 emanating from collapse-1 (see 'Impingement-1' in figure 7*a* and 'Collapse-1' in figure 7*c*). The upper part of the cavity gets completely condensed, while the lower part is partially condensed. To this end, the vapour production rate is high enough for the cavity to keep growing near the throat. However, the pressure wave due to the implosion of the cloud from the previous cycle ('Collapse 2' in figure 7*c*) is already travelling upstream. The propagating shock front (CSF-2) impinges on the cavity at 'Impingement-2' and condenses the vapour it comes across (see figures 7*a*,*b*). Further, it encounters a growing cavity front leading to 'Impingement-2.2' as shown in figure 7(*a*). Consequently, the propagating velocity

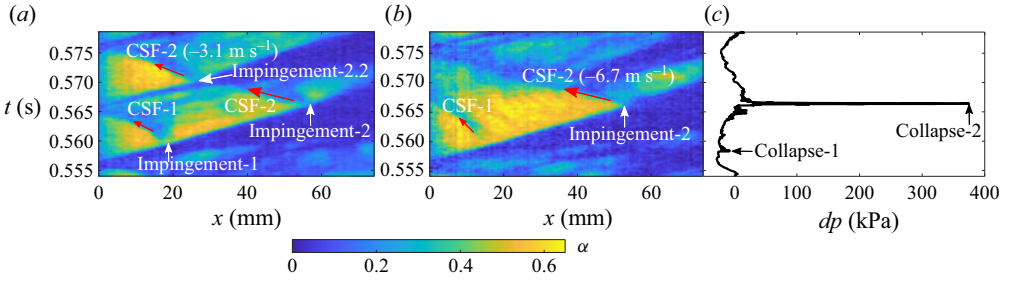

Figure 7. A shedding cycle at $\sigma = 0.47$, showing multiple condensation shock fronts (CSF). (*a*) The upper part of the vapour cavity. (*b*) The lower part of the cavity. (*c*) The *dp* time trace is recorded simultaneously at station p_6.

of the shock front reduces significantly from -6.7 m s^{-1} to -3.1 m s^{-1}. This leads to the condensation shock fronts experiencing two distinct velocities, as evident from the two different slopes of CSF-2, shown in figure 7(*a*). This suggests that the condensation shock front, after Impingement-2.2 (see figure 7*a*) has to overcome the strong vaporisation (cavitation) brought about by the low pressure at the throat. The above anomalous shedding cycles may cause cycle-to-cycle variations; however, the condensation shock front due to the larger pressure pulse is seen to enforce a strong periodicity in the cavity shedding dynamics. This was confirmed by a matching sharp peak in the fast Fourier transform (FFT) of pressure and vapour fraction time series at such σ (see figure 19 in Appendix A).

As the cavitation number increases ($\sigma = 0.78$), we observe slightly different cavitation dynamics with respect to the bubbly shock front. The vapour cavity grows linearly as shown in figures 8(*a*)–8(*c*). The cavitation cloud shed from the previous cycle, shown in figure 8(*b*), will implode in the downstream region. However, the cloud collapse appears less coherent, as is evident from multiple small peaks around the main peak, giving rise to a low-pressure rise ($dp \sim 120$ kPa) recorded at the p_5 location (see figure 8*j*). The cloud implosion gives rise to the upstream travelling pressure wave that impinges on the growing attached cavity, arresting the cavity growth. The impingement is evident from the change in the slope of the cavity front at the impingement point, as shown by the two black dashed lines in figure 8(*i*). The 'bubbly shock wave' is seen to propagate through the cavity without significant condensation, as shown by snapshots in figures 8(*d*,*e*) and a white dotted line in the *x*–*t* plot (see figure 8*i*). The pressure wave can propagate through the cavity if the shock front is subsonic (Brandao *et al.* 2019). As it travels further upstream, it begins to condense the cavity (see again the red arrow in figures 8*f*,*g*). See also supplementary movie 2. The shock front can be seen more clearly by the emergence of a sharp change in the vapour fraction across the travelling front, as shown by the red dashed curve in figure 8(*i*). This coincides with the observed acceleration of the shock front as it approaches the venturi throat, inferred from the changing slope of this red dashed curve. The condensation front then travels upstream until it reaches the throat, resulting in complete cavity condensation and eventual shedding.

At higher cavitation numbers ($\sigma = 0.84$), two different types of shedding cycles are seen. In a few cycles, a pressure wave transformed into a condensation shock front is seen to cause cavity destabilisation, similar to $\sigma = 0.78$ (see figure 9). In other cycles, the cavity dynamics differ, as shown in figure 10. The vapour cavity grows linearly in time (figures 10*a*–*d*). At the instance marked *e* in figure 10(*j*), the cloud implosion from the previous cycle gives rise to an incoherent and lower pressure rise ($dp \sim 60$ kPa).

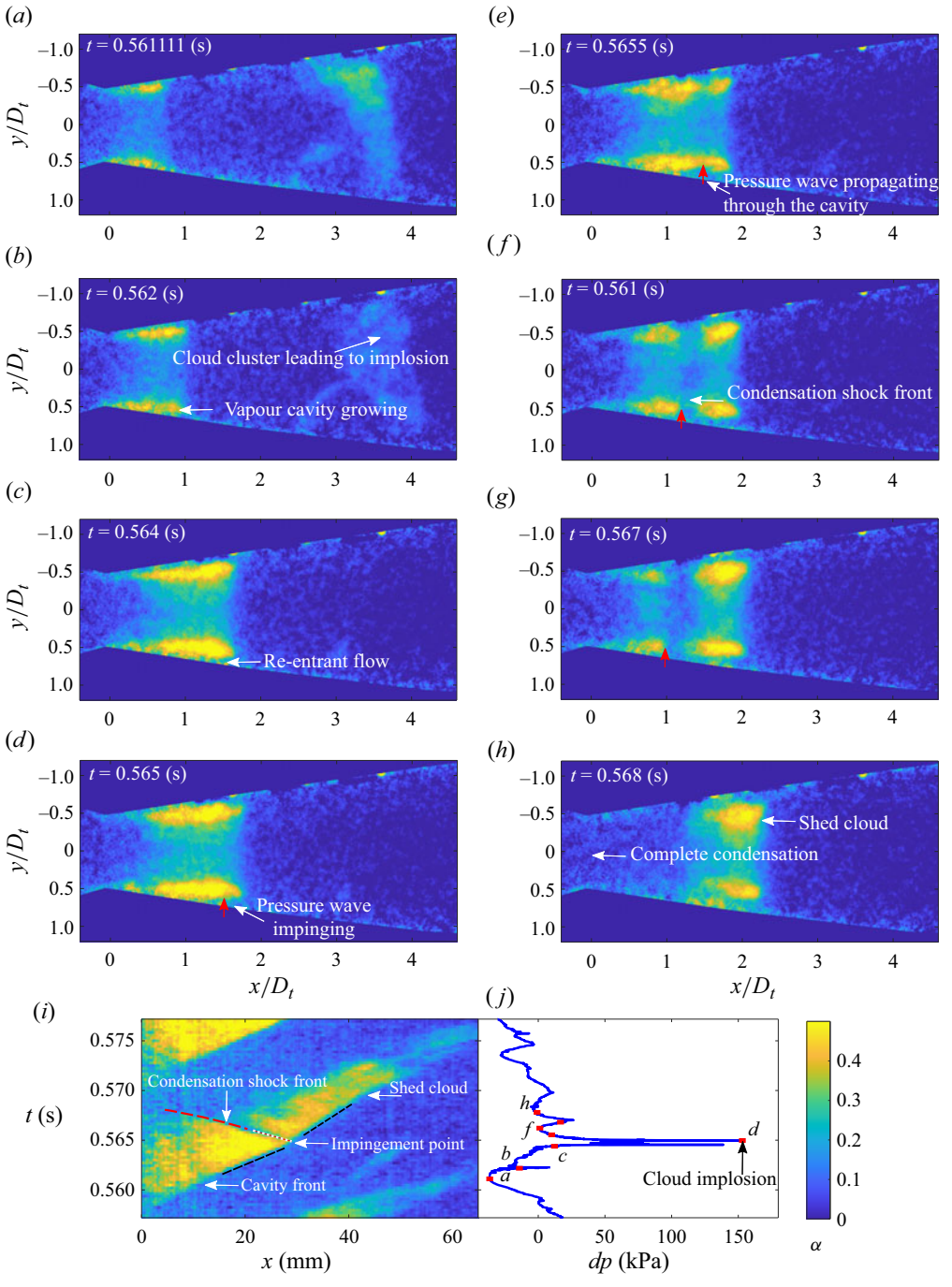

Figure 8. (*a–h*) A single shedding cycle for the case $\sigma = 0.78$. (*i*) The x–t evolution of the vapour fraction of the cavity. (*j*) The dynamic pressure corresponding to this cycle recorded simultaneously at station p_5.

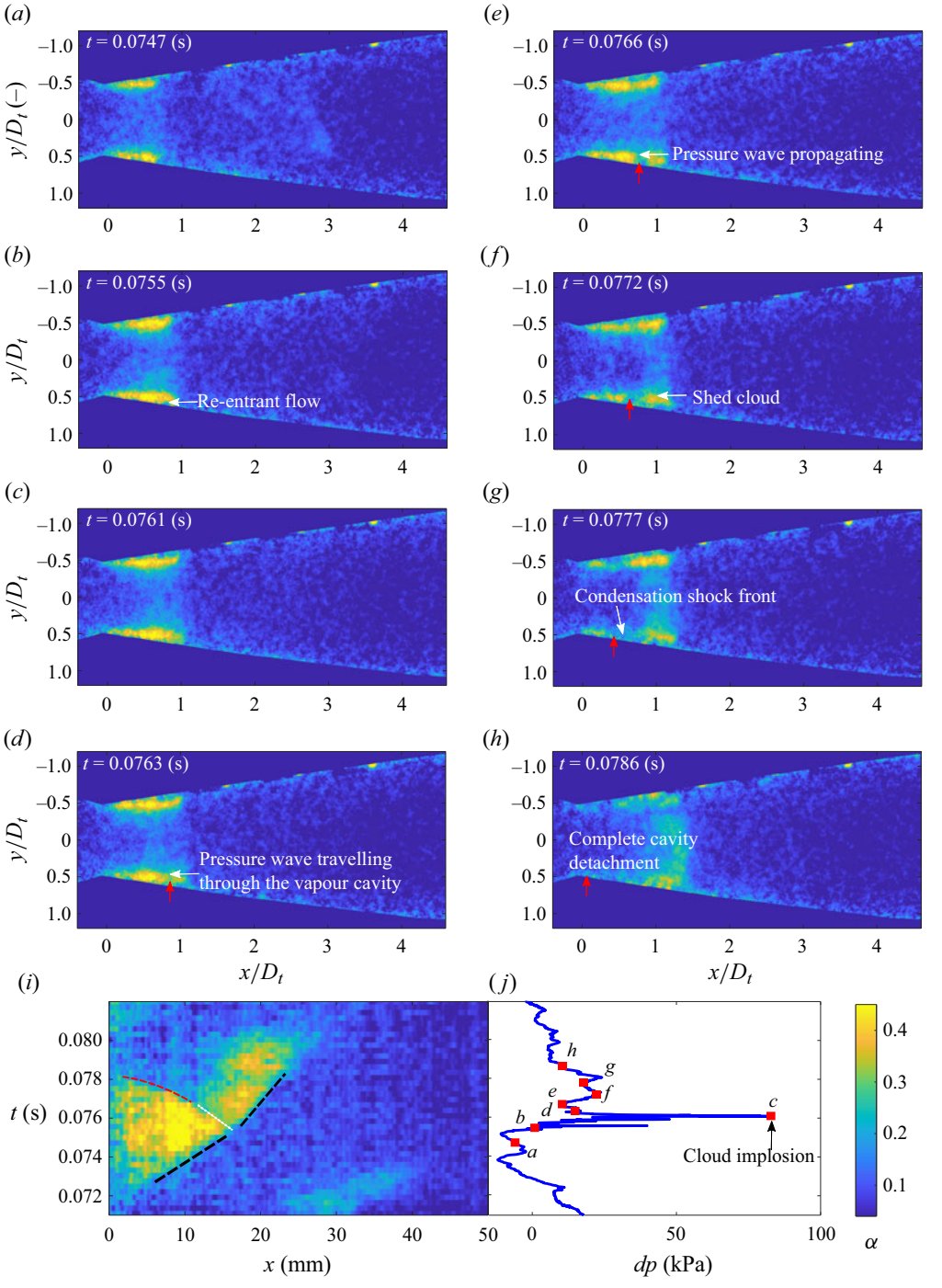

Figure 9. (*a–h*) A single shedding cycle for the case $\sigma = 0.84$. (*i*) The *x–t* evolution of the vapour fraction of the cavity. (*j*) The dynamic pressure corresponding to this cycle recorded simultaneously at station p_5.

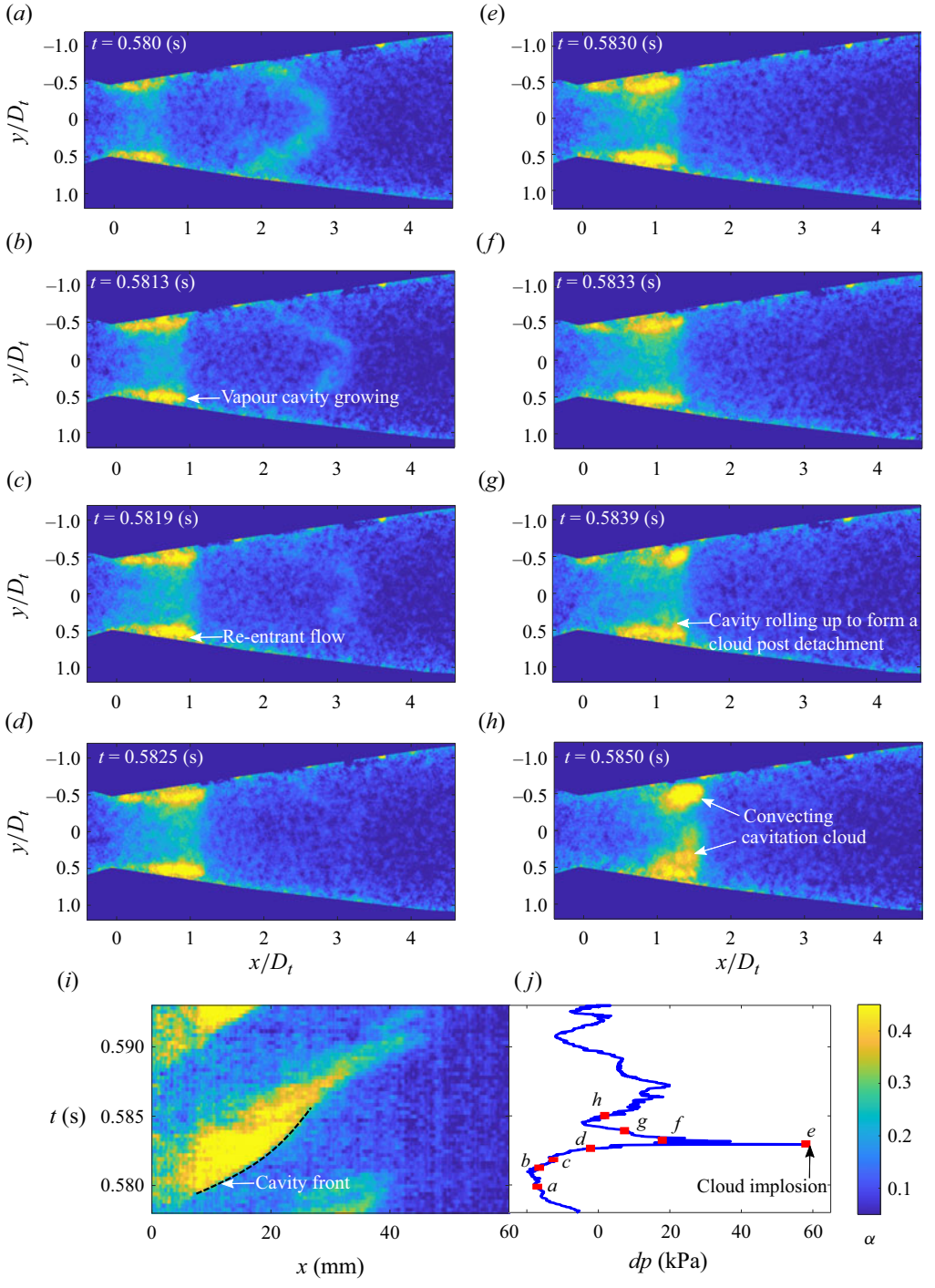

Figure 10. (*a–h*) A single shedding cycle for the case $\sigma = 0.84$. The layout is the same as in figure 9. The dynamic pressure is recorded at station p_4.

The dynamic pressure time trace is recorded at location p_4. The upstream travelling pressure wave cannot be seen impinging on the growing cavity in the x–t diagram in figure 10(i). Moreover, the slope change of the cavity front growth is smoother and not abrupt as in the previously considered cases $\sigma = 0.47$ and 0.78. This is shown by a black dashed curve in figure 10(i). There is no sharp upstream travelling vapour fraction discontinuity in the x–t evolution of the cavity following the cloud implosion, as is clear from figure 10(i). It can be hypothesised that the pressure wave propagates upstream through the attached cavity without condensing it. Thus there is no significant effect of the cloud implosion on cavity growth and detachment. Instead, we observe that the cavity gets pinched off near the venturi throat (see figure 10h) and rolls up to form a convecting cloud, similar to shedding brought about by the re-entrant jet travelling beneath the cavity. This can be seen in supplementary movie 3. With further increase in σ ($= 0.90$), most shedding cycles are seen to be destabilised by the re-entrant jet. It was also shown previously by Gawandalkar & Poelma (2022) that there is a strong upstream-travelling re-entrant jet below the cavity in the same flow geometry at these higher σ.

It is important to stress that these two types of cavity shedding mechanisms are fundamentally different. At low σ, the cavity gets condensed and fragmented by the condensation front before the new cavity starts growing. However, at high σ, a strong re-entrant jet below the vapour cavity pinches the cavity before the new cavity starts growing. It is confirmed in our study that the likelihood of the re-entrant jet causing cavity shedding increases with the increase in σ, as also shown recently by Bhatt, Ganesh & Ceccio (2023). Pressure waves due to cloud implosions are present at all σ (Gawandalkar & Poelma 2022). These observations suggest that both pressure waves emanating from the cloud implosion and re-entrant jets are present to destabilise the attached cavity for a given σ. However, the way in which the pressure wave interacts with the attached cavity dictates the dominant shedding mechanism. At low σ ($\lesssim$0.78), the pressure wave gets transformed into a condensation shock front in nearly every shedding cycle, condensing and fragmenting an attached cavity. However, at $\sigma \sim 0.84$, the pressure wave cannot transform into a condensation shock in all the shedding cycles. In these cycles, the attached cavity is destabilised by a re-entrant jet. With an even further increase in σ ($\sim$0.97), the attached cavity is destabilised solely by the re-entrant jet, as shown previously by Gawandalkar & Poelma (2022). The correlation between the pressure peaks due to cloud collapse and cavity detachment is further established by computing the dominant frequency of the α and dp time signals for a range of σ, as discussed in Appendix A. Further, the time scale of the condensation shock front is in agreement with the global shedding frequency at low to moderate σ, as presented in Appendix B.

3.4. *Characteristics of bubbly shock waves*

In order to understand the above-mentioned shedding behaviour(s), it is imperative to understand the interaction of the pressure waves with the attached vapour cavity. Thus we characterise the bubbly shock waves travelling through the cavity. In particular, we use the vapour fraction pre-shock front (α_1), the post-shock front (α_2), the pressure rise across the shock front (Δp), the velocity of the condensation shock front (u_{sw}), and the Mach number (Ma_{sw}) to characterise the bubbly shock waves. Further, all the quantities are phase-averaged using the approach detailed in Gawandalkar & Poelma (2022). The standard deviation of the phase average is expressed as error bars. The error bars can be attributed mainly to the cycle-to-cycle variation in shedding dynamics along with random noise in the measurement.

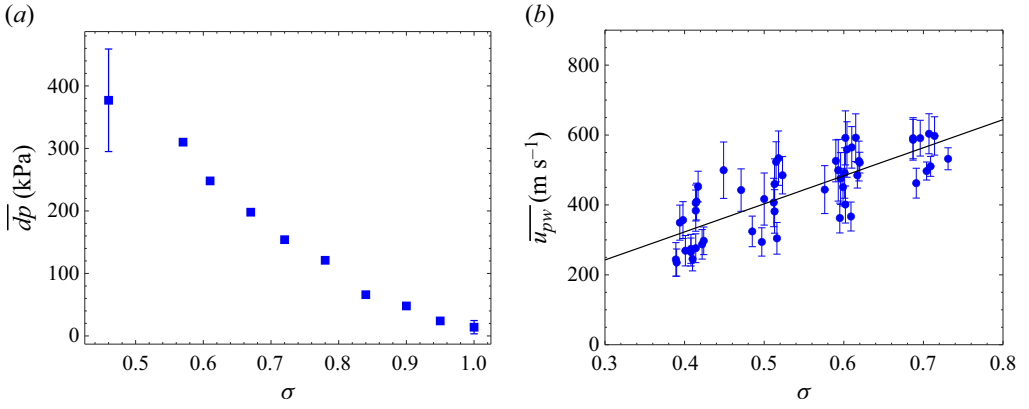

Figure 11. (*a*) The phase-averaged pressure rise due to the cloud implosion recorded in the pressure recovery section (p_4, p_5 or p_6, whichever is closest to the location of the cloud implosion) for a range of σ. (*b*) The phase-averaged velocity of the pressure wave travelling through the liquid measured using dynamic pressure transducers at p_4 to p_6.

The pressure wave emanates from cloud collapse/implosion in the downstream region of the venturi. This is inferred from the sharp peak in the dynamic pressure (dp) signal during the shedding process (see figures 5*j*, 8*j*, 10*j*). The pressure peak brought about by the cloud implosion is recorded by the transducer closest to the collapse location (p_4, p_5 or p_6; see figure 1(*c*) for a schematic). It can be seen that the phase-averaged pressure peak ($\overline{dp}$) decreases significantly with increasing σ, as shown in figure 11(*a*). The pressure wave propagating through the low vapour fraction region is detected as a pressure discontinuity by transducers at the p_4 to p_6 locations. The availability of multiple transducers allows us to track this pressure discontinuity in time. The time delay between the peaks and the distance between the transducers are used to estimate its velocity of propagation ($\overline{u_{pw}}$). The pressure wave is seen to propagate at a velocity that is an order of magnitude higher than the bulk velocity (U_t), as shown in figure 11(*b*). This pressure wave, after impinging on the cavity, interacts with it, i.e. condenses it. The pressure rise (Δp) associated with this bubbly shock wave is recorded using multiple pressure transducers, located at p_1, p_2 and p_3. The magnitude of the pressure rise is measured as the shock front propagates through the attached vapour cavity.

An example of the pressure wave dynamics and its interaction with the growing cavity is shown for $\sigma = 0.67$ in figure 12. The collapsing cloud is shown in figures 12(*a*) and 12(*b*). Note that the collapse takes place to the right-hand side of the p_3 location, which in this case falls within our FOV. The pressure wave emanating from this implosion propagates upstream through the liquid and is first picked up by the pressure transducer at p_3; see the sharp peak (marked as *b*) in the red dp signal in figure 12(*g*). Further, this discontinuity is seen to propagate through the vapour cavity as a condensation shock front (marked by red arrows), as identified near p_2 in figure 12(*d*) and p_1 in figure 12(*e*). This coincides with the pressure rise at p_2 (marked *d* in the green time signal) and p_1 (marked *e* in the blue time signal), as shown in figure 12(*g*). It is important to note that the condensation shock front appears somewhat obscure in these high-speed images, necessitating vapour fraction measurements as in this study. The pressure rise (Δp) at p_1 appears to be higher than the pressure rise at p_2. This will be addressed in § 3.7. It is observed that the pressure discontinuity (Δp) across the condensation front is weaker, i.e. the pressure rise is almost one order of magnitude lower than the pressure peak (dp) due to

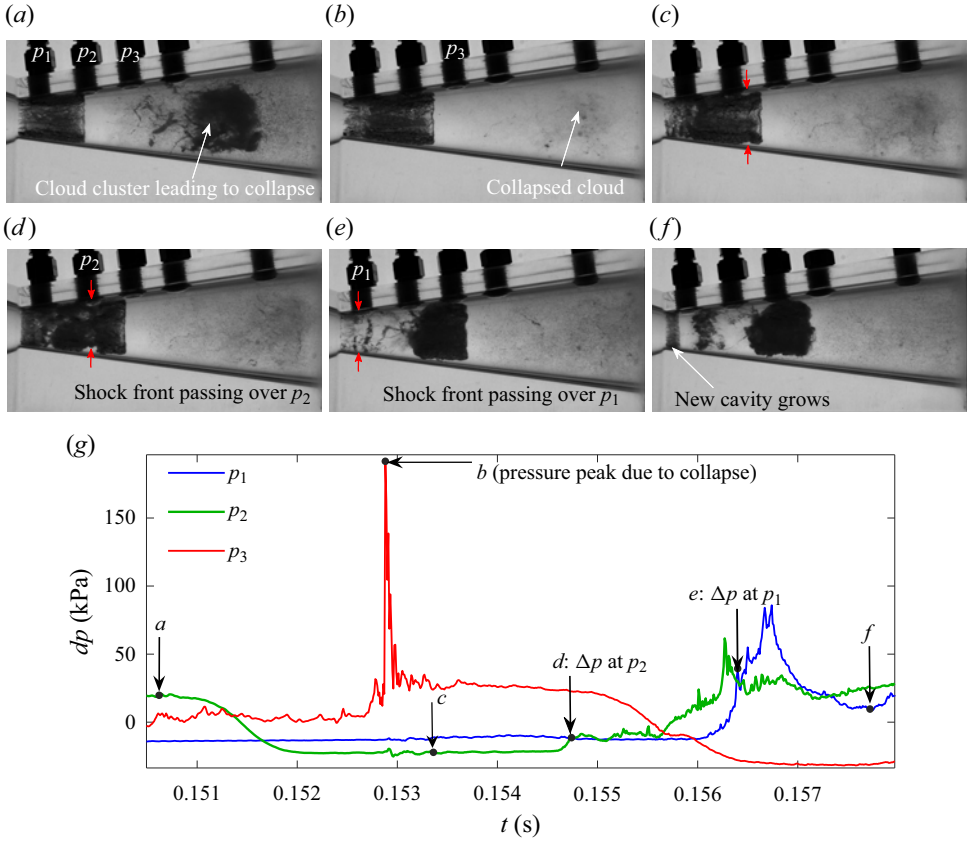

Figure 12. (*a–f*) High-speed shadowgraphs showing the propagation of the condensation shock front through the vapour cavity at $\sigma = 0.67$ (red arrows show the bubbly shock wave signature). (*g*) The corresponding dynamic pressure time series at three axial locations (p_1, p_2, p_3) exhibit the pressure rise brought by it.

the cloud implosion. The phase-averaged Δp across the condensation front decreases with increasing σ, as shown in figure 13(*a*). Thus the pressure rise caused by the condensation shock front at higher σ is lower, indicating that the strength of the condensation shock front is decreasing with increasing σ. This then coincides with the condensation shock front becoming a less dominant shedding mechanism, as illustrated by the observed shedding dynamics.

The vapour fraction is quantified using time-resolved X-ray densitometry, as mentioned with an uncertainty of less than 5 %. The vapour fractions on either side of the condensation shock front (red dashed curve in figures 5*i*, 8*i*, 9*i*) are expressed as α_1 and α_2 (see also inset in figure 13*c*). The vapour fraction ahead of the condensation shock front (α_1) varies from 0.83 to 0.45, with a variation of σ from 0.39 to 0.84. So α_1 decreases monotonically with σ. However, the post-shock vapour fraction is almost constant at $\alpha_2 \sim 0.1$, as shown in figure 13(*b*). Thus there is a strong gradient of vapour fraction across the shock front, suggesting rapid condensation of the vapour cavity by the propagating condensation shock front. Further, the measured vapour fraction values are in agreement with the vapour fractions reported by Ganesh *et al.* (2016). The velocity of the shock front in the laboratory frame of reference is estimated by computing the inverse of the gradient to the linear part of the shock front identified in the *x–t* plot (see red markers in figure 13*c*).

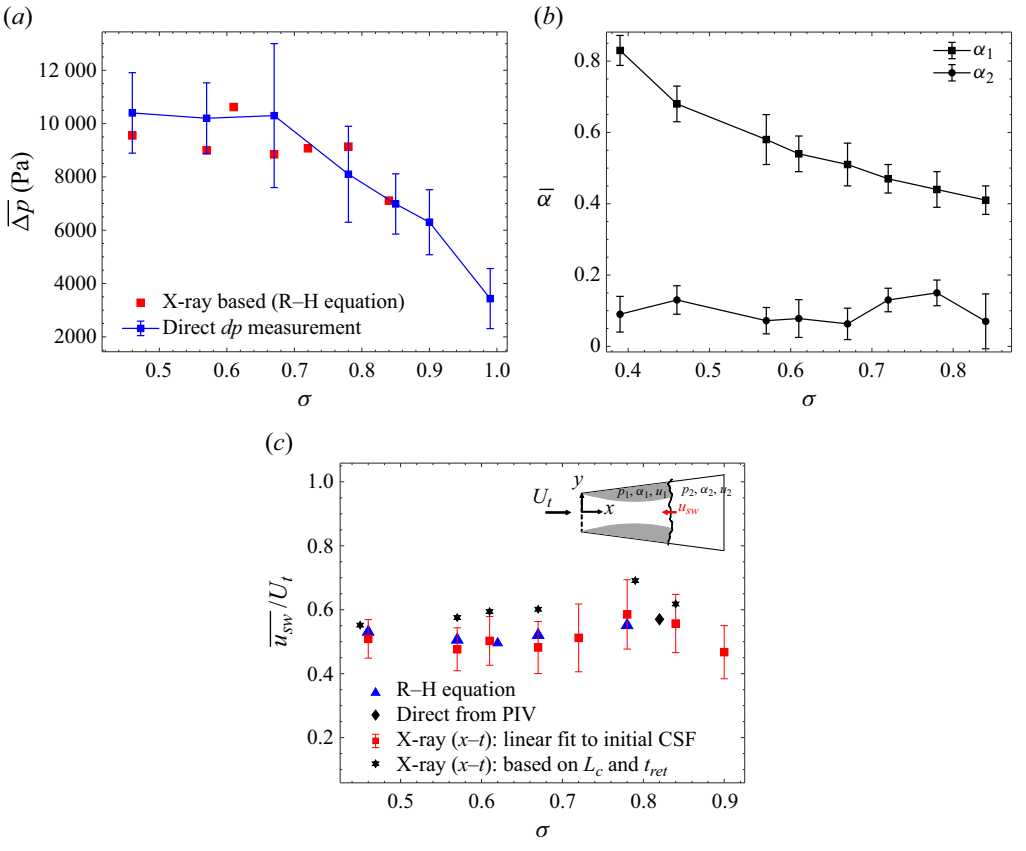

Figure 13. Characteristics of the bubbly shock waves. (*a*) The phase-averaged pressure rise recorded across the condensation shock front travelling through the attached vapour cavity (p_1 to p_3). The red markers show the pressure rise predicted using the measured shock front velocity and vapour fractions using (3.1). (*b*) Phase-averaged vapour fraction, pre (α_1) and post (α_2) shock front. (*c*) Phase-averaged condensation shock front velocity (u_{sw}) normalised with the throat velocity (U_t). Blue markers indicate the velocity predicted with the Rankine–Hugoniot (R–H) equation (u_{rh}), red markers indicate the velocity computed by fitting a straight line to the condensation shock front in the x–t evolution of α, star markers indicate the shock front velocity obtained by L_c/t_{ret}, and the diamond marker indicates the velocity of the shock front measured directly using PIV by Gawandalkar & Poelma (2022).

The linear fit to the shock front follows the previous studies of Ganesh *et al.* (2016) and Budich *et al.* (2018). Alternatively, the shock front velocity ($\sim L_c/t_{ret}$) is also determined using the length of the vapour cavity through which it travels (L_c) and the time it spends in the cavity (t_{rec}; see Appendix B). These are shown by *star* markers in figure 13(*c*). They are consistently somewhat higher than the previous velocity estimates, suggesting that the condensation shock front velocity is not constant; rather, it accelerates as it approaches the throat. This is in agreement with direct PIV measurements by Gawandalkar & Poelma (2022). The acceleration will be addressed in detail in § 3.7. Despite a relatively large variation in α_1, the shock front velocity at different σ is almost constant when normalised by U_t, i.e. $\sim 0.55U_t$. Interestingly, it is close to the maximum velocity of the re-entrant jet in a shedding cycle reported by Gawandalkar & Poelma (2022). Further, u_{sw} is almost two orders of magnitude lower than u_{pw}, as shown in figures 11(*b*) and 13(*c*).

Measurements of Δp and vapour fraction (α_1, α_2) are validated with each other using a one-dimensional Rankine–Hugoniot (R–H) equation, given by (Brennen 1995)

$$u_{rh}^2 = \frac{\Delta p}{\rho_l}\left[\frac{(1-\alpha_2)}{(1-\alpha_1)(\alpha_1-\alpha_2)}\right]. \tag{3.1}$$

Here, all the symbols have previously defined meanings. The R–H equation is derived using mass and momentum conservation along with the binary mixture model for density. The shock front velocities predicted with measured α_1, α_2, Δp using the R–H equation (blue markers in figure 13*c*) show excellent agreement with the estimated values from *x*–*t* plots (red markers in figure 13*c*). Further, Δp predicted with measured α_1, α_2 and u_{sw} using (3.1) (red markers in figure 13*a*) agrees with direct Δp measurement.

3.5. *Cavity pressure*

The absolute pressure inside the vapour cavity is cumbersome to measure experimentally. Thus to get a ballpark estimate of the pressure inside the cavity, we measure the pressure at the venturi wall, at a location p_1 (see figure 1). This pressure at a single point is used as a proxy for the whole cavity pressure. The unsteady total pressure measurement is time-synchronised with high-speed imaging. This is done to discount the pressure time signal where the pressure transducer is not covered by the cavity. Further, the periodic, sharp pressure peaks caused by the cloud implosion downstream are filtered out using a low-pass filter. This is followed by time averaging the pressure signal for 10 s to yield the cavity pressure (P_c). It is seen that P_c can be higher than the vapour pressure (P_v). However, at a lower cavitation number (σ), the pressure is seen to approach P_v (see figure 14). This can be attributed to the bubbly nature of the cavity, where the vapour fraction increases with a decrease in the cavitation number. For a given static pressure in the system, the pressure is seen to be decreasing monotonically with the increase in the free-stream velocity. Naturally, with the decrease in the global static pressure, the absolute pressure inside the cavity decreases. The absolute pressure, when normalised by the dynamic pressure at the throat, collapses on a curve, suggesting that σ and U_t are sufficient to estimate the pressure inside the cavity (see the inset in figure 14). The pressure of the bubbly cavity mixture will be used to estimate the speed of sound in such a mixture.

3.6. *Mach number of the condensation shock front*

It is well known that the speed of sound is significantly lower in a bubbly mixture than in pure liquid or vapour (Prosperetti 2015; Shamsborhan *et al.* 2010). The cavity having substantial vapour fractions (0.4–0.8; see figure 13*b*) can reduce the speed of sound, rendering the medium compressibility important. Thus with the measured vapour fraction (α_1) and the pressure of the bubbly mixture of the cavity (P_c), we can now make a rough estimate of the speed of sound in the cavity (c_m) using (Brennen 1995)

$$c_m = \left\{\left[\frac{\alpha_1}{kP_c} + \frac{1-\alpha_1}{\rho_l c_l^2}\right][\alpha_1\rho_v + (1-\alpha_1)\rho_l]\right\}^{-1/2}. \tag{3.2}$$

It is assumed that the cavity is a homogeneous bubbly mixture, and water vapour behaves as a perfect gas with the polytropic gas constant k. Further, the bubble dynamics in the cavity such as coalescence and surface tension are omitted for simplicity. Here, ρ is the mass density, and c is the speed of sound in the medium; subscripts v and l are used for

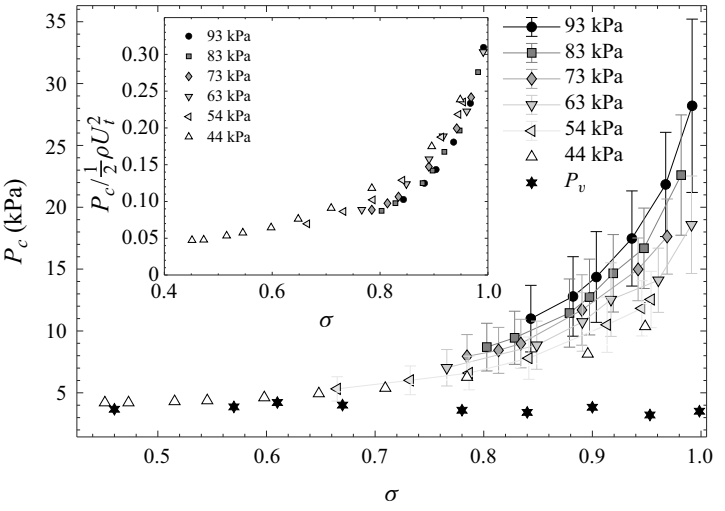

Figure 14. Conditionally phase-averaged static pressure inside the cavity (P_c) measured at location p_1 as a function of the cavitation number (σ) for different global static system pressures; P_v refers to the vapour pressure. The inset shows the pressure normalised with the incoming dynamic pressure.

vapour and liquid, respectively. The mixture pressure (P_c) is estimated in the previous subsection. The Mach number of the shock front (Ma_{sw}) can now be estimated with the speed of sound (c_m) and u_{sw}, as

$$Ma_{sw} = \frac{\overline{u_{sw}}}{c_m}. \tag{3.3}$$

Since we are interested in the interaction of the pressure wave with the bubbly cavity when it impinges on it, the phase-averaged condensation shock front velocity estimated in figure 13(*c*) is used to estimate the Mach number (Ma_{sw}). Figure 15 shows that Ma_{sw} decreases with increasing σ, further corroborating that the strength of the condensation shock travelling through the cavity is decreasing with increasing σ. Such behaviour of the condensation shock front was also reported by Ganesh *et al.* (2016) and Bhatt & Mahesh (2020) for a two-dimensional wedge and backward-facing step geometry, respectively. We see that Ma_{sw} is greater than unity, i.e. it is supersonic for lower σ. However, it falls below or hovers close to unity for higher σ ($\sim$0.90). At even higher σ, the condensation shock fronts were not observed in our study. Thus $Ma_{sw} \sim 1$ coincides with the disappearance of condensation shock fronts. This suggests that the pressure and vapour fraction fields at higher σ render the bubbly shock wave weaker and likely subsonic. This weakening of the shock front is likely to mitigate the complete condensation of the cavity at higher σ, as opposed to lower σ, where the pressure wave completely condenses the cavity. This is in line with observed cavity dynamics at $\sigma \sim 0.84$ and 0.90, where most shedding cycles begin to show re-entrant jet-driven shedding. With further increase in σ ($\sim$0.97), all the shedding cycles were destabilised by the re-entrant jet, as shown previously by Jahangir *et al.* (2018) and Gawandalkar & Poelma (2022). Thus the shedding mechanism switches from a condensation shock front to a re-entrant jet as the pressure wave emanating from the cloud implosion becomes weaker.

In summary, it is evident that the Mach number of the bubbly shock front (Ma_{sw}) decreases as σ increases, suggesting that the pressure wave travelling through the vapour cavity appears to get weaker with increasing σ. This is corroborated by the observed

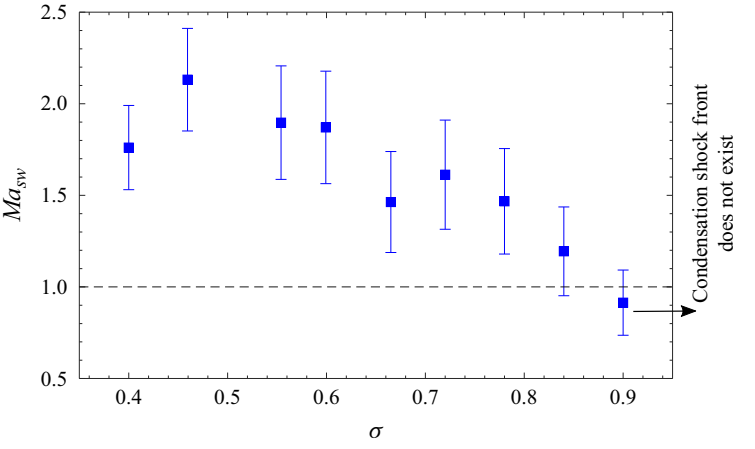

Figure 15. The Mach number of the condensation shock front (Ma_{sw}) as a function of the cavitation number (σ). The black dashed line shows $Ma_{sw} = 1$.

cavity shedding dynamics, i.e. at $\sigma = 0.47$: the impinged pressure wave starts immediately condensing the cavity. At intermediate $\sigma = 0.78$, a condensation shock front emerges as the pressure wave propagates upstream. However, at $\sigma = 0.84$, the pressure wave appears to be too weak to condense the cavity readily. Thus the pressure wave is expected to propagate through the cavity without condensing it for the majority of the cycles. At this σ, a strong re-entrant jet is also present below the cavity, as shown by Gawandalkar & Poelma (2022). Therefore, the re-entrant jet takes over as the dominant cavity detachment mechanism for higher σ. The velocity of the condensation shock front and re-entrant jet is of the same order of magnitude. If the pressure and the vapour fraction of the bubbly cavity allow the condensation of the cavity, then the phase change from vapour to liquid will dictate the cavity destabilisation. Alternatively, the cavity pinch-off by the re-entrant jet is favoured. Therefore, it is seen that the pressure field and the shock wave characteristics have a strong influence on the prevalence of the dominant shedding mechanism.

3.7. *Kinematics of the condensation shock front*

As stated in the previous subsection, the condensation shock front is seen to accelerate as it travels upstream towards the venturi throat. This can also be seen in previous studies, for instance, in the x–t diagram showing the cavity dynamics in the experiments of Wu *et al.* (2019) and the large eddy simulations of Bhatt & Mahesh (2020). However, due to the low flow blockage in those studies, the acceleration is suspected to be not severe. As a result, it has not received much attention. In the current flow geometry, the flow blockage ratio is ∼9, which is significantly higher. Further, it is seen that at intermediate cavitation numbers ($\sigma \sim 0.78$–0.84), the emergence of a sharp condensation shock front coincides with the observed acceleration of the shock front. Thus it is imperative to account for the effect of acceleration of the condensation shock front in the present context. The velocity of the condensation shock front as a function of axial distance (x) is evaluated by computing the phase-averaged gradient to the measured condensation shock front in the x–t diagram (see figure 16). The phase averaging of $u_{sw}(x)$ is performed over so-called 'clean cycles' (∼80 %), omitting shedding cycles with local variations such as sudden acceleration or multiple condensation shock fronts. The error bars indicate the cycle-to-cycle variation in the velocity. The acceleration appears significant: the velocity

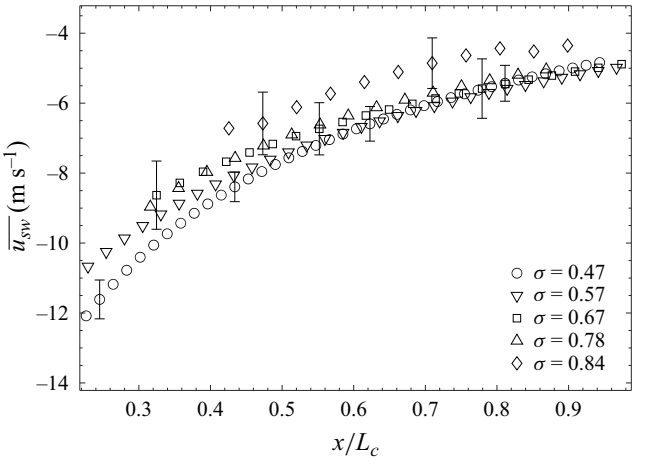

Figure 16. The shock front velocity ($\overline{u_{sw}}$) plotted against x normalised by the maximum cavity length (L_c).

doubles in half the cavity length. The acceleration experienced by the shock front while travelling upstream could be attributed to the axial variation of vapour fraction across the shock front ($\alpha_1(x)$), the change in the cross-section of the venturi as seen by the shock front, or the change in pressure of the cavity. Due to the difficulty in measuring experimentally the pressure inside the cavity, the pressure is assumed to be constant. The axial variation of the vapour fraction ($\alpha_1(x)$) encountered by the travelling shock front is shown for three σ values (see figure 17*a*). The axial variation is negligible ($\lesssim 0.07$) and within the measurement uncertainly. Further, we check if the shock front is accelerating due to the converging walls of the venturi (from the shock front frame of reference, given that it is travelling upstream). In that case, the measured shock wave velocity must vary to obey the mass conservation imposed by the geometry. This can be used to construct a simple model based on one-dimensional mass conservation and the initial shock front velocity to predict the velocity variation. The measured phase-averaged shock front velocity ($\overline{u_{sw}(x)}$) variation with x is shown by markers in figure 17(*b*). It is observed that the agreement with predictions (dashed lines in figure 17*b*) is good. However, closer to the throat, the agreement appears worse. This can be attributed to assumptions made in the model such as constant pressure and density, and the difficulty in defining the condensation shock front close to the throat. Considering this, we can safely attribute the acceleration to the converging walls of the venturi as seen by the shock front.

Further, we examine if this increasing velocity of the shock front has an effect on the dynamics of the condensation shock wave. We measure Δp brought about by the condensation shock front as it travels upstream. The Δp measurements are done at multiple axial locations, p_1, p_2 and p_3 (see figure 1(*c*) for the locations). Interestingly, at $\sigma = 0.47$, the pressure rise of the shock front (Δp) at p_2 is 10.38 kPa, which increases to 17.01 kPa at p_1. Similarly, at $\sigma = 0.67$, the pressure rise increases from 10.32 kPa (at p_2) to 13.60 kPa (at p_1). Thus the pressure rise across the bubbly shock front is seen to increase as it propagates upstream. Finally, we estimate the Mach number of the accelerating condensation front, $M_{sw}(x)$, as it travels upstream through the bubbly vapour cavity (see figure 18). It is assumed that the pressure of the bubbly mixture through which the condensation front travels is constant. Further, the vapour fraction that it encounters is nearly constant, as shown in figure 17(*a*). Thus the speed of sound is also assumed to be constant, in accordance with (3.2). It is seen that at the lowest cavitation number

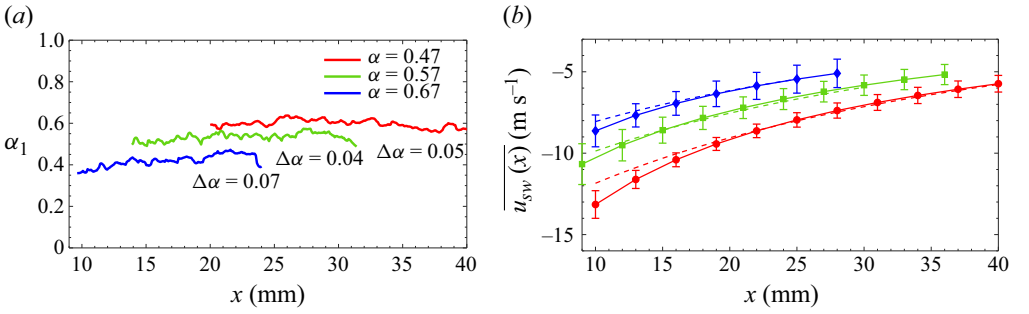

Figure 17. (*a*) The pre-shock vapour fraction (α_1) plotted against x. (*b*) The axial variation of the phase-averaged shock wave velocity ($\overline{u_{sw}}$, markers) compared with velocity predictions by mass conservation (dashed lines) at different σ (same colour coding as in (*a*)). Every third data point is shown for clarity.

($\sigma \sim 0.47$), the bubbly shock front is supersonic as it impinges on the cavity and remains supersonic as it travels through the cavity. This results in complete condensation of the cavity, as also observed in the time series shown in figure 5. The complete condensation is evident from the sharp jump in the vapour fraction over the entire shock front, as shown in figure 5(*i*). As the cavitation number increases ($\sigma = 0.78$), the bubbly shock wave is initially subsonic as it impinges on the cavity, until $x/L_c \sim 0.89$, as shown in figure 18. This is also seen in the vapour fraction time series (see figure 8), where the pressure wave front is seen to travel through the cavity without condensing it. However, as it accelerates while travelling upstream, it becomes supersonic at $x/L_c \sim 0.84$ (corresponding to $x =$ 21.2 mm in the x–t diagram shown in figure 8*i*) and starts complete condensation of the vapour cavity. Thus the axial location where the pressure wave becomes subsonic agrees well within the measurement uncertainty. At even higher σ (∼0.84–0.90), the pressure wave cannot become supersonic readily (see figure 18). This can also be seen in the shedding dynamics shown in figure 9(*i*): the shock front inferred from a sharp change in α appears further upstream. At such a flow condition, the pressure wave after impinging on the vapour cavity is less likely to condense it, allowing the re-entrant jet below the cavity to pinch it off. This shows the effect of the kinematics of the shock front on the cavity shedding dynamics.

The phenomenological description of the vapour cavity shedding in an axisymmetric venturi for intermediate σ can be given as follows. The pressure wave emanating from the previous cloud implosion impinges on the growing cavity. However, the velocity of the pressure wavefront (u_{sw}) and the pressure rise across it (Δp) are not enough to condense the cavity, i.e. it is likely subsonic. As the pressure wave travels upstream, its velocity increases due to the converging geometry of the venturi (blockage). Consequently, the pressure rise across it also increases. This makes the shock front stronger or even supersonic, favouring condensation. At lower σ, the impinging pressure discontinuity is supersonic. Hence the condensation shock front is seen to exist over the entire cavity length. However, at high σ, the pressure discontinuity is weak and remains subsonic, despite the acceleration. Thus it appears that the effect of such a flow geometry with a large blockage is to accelerate the pressure wave, increasing its strength as it travels upstream. This, in turn, explains the large range of cavitation numbers ($\sigma \sim 0.30$–0.78) for which the condensation shock front is the dominant cavity destabilising mechanism, as opposed to the re-entrant jet, which is seen to occur only for $\sigma \sim 0.95$–1.1.

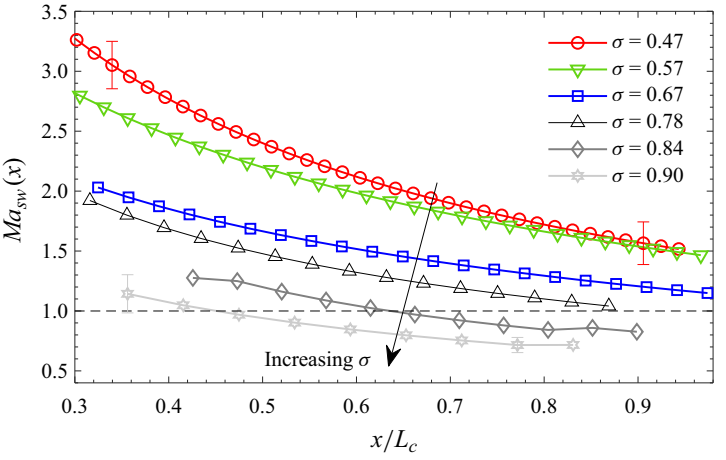

Figure 18. The Mach number (Ma_{sw}) variation of the bubbly shock front with the axial distance (x) normalised by cavity length (L_c) for different cavitation numbers (σ). The direction of propagation of the shock fronts is upstream, i.e. to the left in this figure.

4. Summary and conclusions

Partial cavitation in an axisymmetric venturi has been studied with time-resolved X-ray densitometry, in combination with high-frequency pressure transducers. The densitometry allows us to circumvent the opacity of the cavitating flow, enabling robust estimations of vapour cavity topology such as cavity length, height and vapour fractions (instantaneous, time-averaged and phase-averaged) at different cavitation numbers (σ). On the other hand, the pressure transducers allow us to detect the pressure discontinuity arising from the cloud collapse and track the pressure wave as it propagates through the attached cavity. The measured static pressure in the cavity in combination with vapour fractions enables us to estimate the speed of sound in a bubbly cavity. This allows us to quantify the Mach number of the shock front.

The primary aim of this study is to examine the interaction of the pressure wave emanating from the cloud implosion with the attached cavity at different flow conditions (σ). This helps us to probe the physics underlying the transition of the cavity destabilising mechanism from re-entrant jet to condensation shock wave in an axisymmetric venturi. This is realised by characterising the pressure wave travelling upstream through the attached cavity at different σ, i.e. vapour fraction (pre-front α_1, post-front α_2), pressure rise (Δp) across the shock front. Further, the velocity of the shock front propagation (u_{sw}) and its Mach number (Ma_{sw}) shed light on the importance of compressibility in such bubbly flows of substantial vapour fraction. Moreover, the pressure pulse propagating in the bubbly liquid (low vapour fraction region) is also characterised. The periodicity in the cavity shedding is leveraged to undertake phase averaging on the quantities. It is seen that the pressure peak (dp) and propagation velocity (u_{pw}) of the pressure wave propagating through a low vapour fraction bubbly mixture are two orders of magnitude higher in comparison to when it propagates through the attached cavity. The upstream propagating pressure wave, when impinging on the cavity, starts condensing it. The pressure rise across the condensation shock front (Δp) is of the order of magnitude $\sim$10 kPa. The vapour fraction of the cavity is in the range 0.4–0.8. Further, the condensation shock front is seen to travel at approximately $\sim 0.55U_t$, which is interestingly of the same order of magnitude as that of the re-entrant jet velocity reported earlier by Gawandalkar & Poelma (2022)

in the same flow geometry. This also means that the time scale of shedding associated with the two shedding mechanisms is similar; however, the shedding mechanisms are fundamentally different.

The cavitation dynamics visualised by the time series of the vapour fraction reveal that the interaction of the pressure wave with the attached cavity at a low cavitation number can be explained as follows. The pressure wave impinges on the cavity. This pressure wavefront is supersonic as the bubbly mixture through which it propagates has a high vapour fraction ($\alpha_1 \sim 0.7$) and low mixture pressure (P_c). The combination of this makes the shock front supersonic ($Ma_{sw} > 1$), which completely condenses the vapour cavity, resulting in its fragmentation and destabilisation. It is also observed that the condensation shock enforces a strong periodicity in shedding, despite local instantaneous events in the shedding process. As the cavitation number increases, the pressure wave impinging on the cavity is weaker and likely subsonic ($Ma_{sw} < 1$). However, as it propagates upstream, it becomes stronger, i.e. supersonic ($Ma_{sw} > 1$), resulting in the onset of cavity condensation. This is evident from the emergence of a sharp gradient in the vapour fraction as the bubbly shock wave propagates upstream. This coincides with an increase in shock front velocity ($u_{sw}(x)$) as it propagates upstream, leading to an increased pressure rise (Δp) across it according to (3.1). The observed acceleration is attributed to the converging walls of the venturi as seen by the shock front. A simple model based on mass conservation is found to predict the acceleration of the shock front fairly well. Thus the kinematics of bubbly shock waves can have a significant influence on their dynamics, which in turn influences the shedding dynamics.

With a further increase in the cavitation number, the pressure discontinuity from the cloud implosion gets even weaker, and despite the acceleration of the shock front, the Mach number of the pressure wavefront seems to remain low or subsonic, i.e. $Ma_{sw} \lesssim 1$. Thus condensation is not favoured readily in the majority of the cycles. This coincides with a strong re-entrant jet existing beneath the cavity in such cycles. They exhibit cavity pinching, cloud detachment and roll-up, typical of cavity shedding triggered by a strong re-entrant jet below the vapour cavity. With an even further increase in cavitation number ($\sigma > 0.95$), all the shedding cycles will be shed predominantly by the re-entrant jet, as shown previously by Jahangir *et al.* (2018) and Gawandalkar & Poelma (2022).

Thus pressure and density/vapour fraction fields in such a bubbly flow have a significant influence on the interaction of the pressure waves with a cavity. This interaction determines if the shock front remains subsonic or becomes supersonic, which in turn influences if the cavity shedding is caused by the bubbly shock wave or the re-entrant jet. Moreover, the effect of a high-blockage flow geometry, such as the axisymmetric venturi, is to strengthen the shock front by accelerating it. This helps to explain the dominance of bubbly shock waves over re-entrant jets as a mechanism driving the periodic cloud shedding in an axisymmetric venturi.

Supplementary movies. Supplementary movies are available at https://doi.org/10.1017/jfm.2024.435.

Funding. This work is funded by the ERC Consolidator Grant no. 725183 'OpaqueFlows'. The authors thank W. Cornel and J. Ruijgrok (TU Delft) for helping to realise experiments at TNO. The authors also thank F. Hilvers, P. Rensink and H. Broos at TNO Ypenburg for hosting us and their cooperation with the HSX facility. Further, the authors thank E. Overmars, G. Mulder and J. Graafland at TU Delft for their technical assistance.

Declaration of interests. The authors report no conflict of interest.

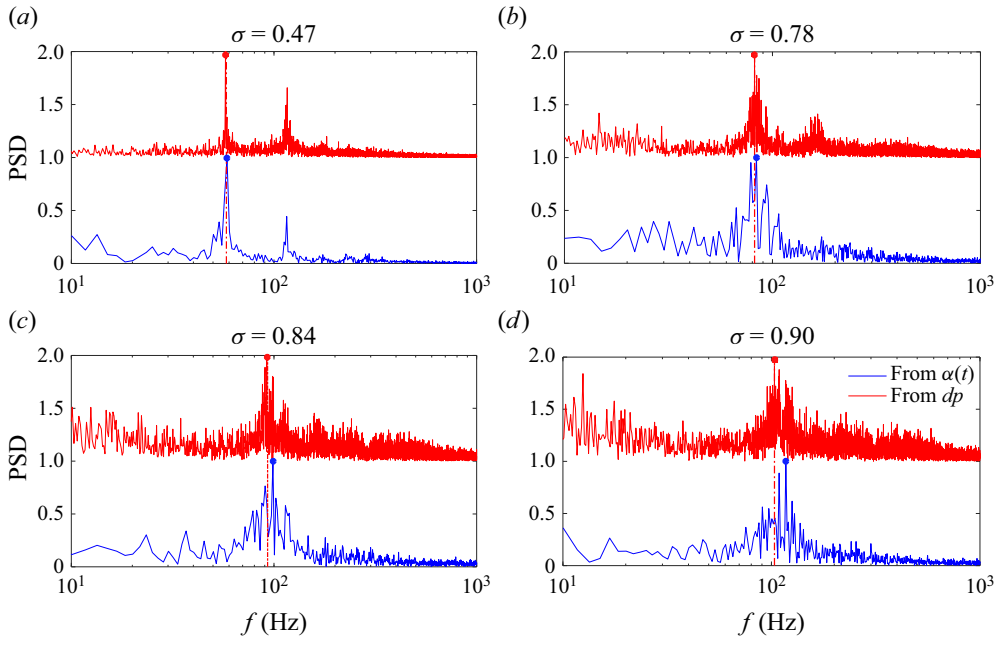

Figure 19. The FFT showing the dominant frequency of vapour fraction $\alpha(t)$ and pressure pulse due to cloud implosion $dp(t)$ for $\sigma = 0.47$, 0.78, 0.84 and 0.90. The red dash-dotted vertical lines indicate the peak in the FFT of dp.

Author ORCIDs.
Udhav U. Gawandalkar https://orcid.org/0000-0002-7638-8721;
Christian Poelma https://orcid.org/0000-0001-8676-9221.

Appendix A. Correlation between pressure peaks and shedding

The correlation between vapour cavity shedding and pressure peaks arising from the cloud collapse is shown by computing the FFT of the dp and α time signals at different σ. For the x–t diagram, several x positions are averaged to estimate the spectral density. Note that dp and α are measured independently in the same experiment. It is seen that for $\sigma \leqslant 0.78$ (see figures 19*a*,*b*), dominant frequencies match accurately, suggesting a good correlation between pressure pulse and cloud shedding via condensation. However, at $\sigma \geqslant 0.84$, there is a small mismatch between peaks (see figures 19*c*,*d*). This is attributed to the pressure waves no longer being strong enough to condense and cause cavity detachment in most cycles. Thus the correlation between pressure peaks due to cloud collapse and cavity detachment appears weaker.

Appendix B. Time scales of the shock front

A typical vapour cavity shedding cycle can be thought of as composed of three parts: (i) cavity growth, (ii) cavity retraction by the condensation shock front and (iii) no cavitation near the throat. An x–t plot of the cavity evolution is an ideal tool to examine the time scales of the shedding process (see figure 20*a*). Here, t_{cg} denotes the time scale for which the cavity grows to its maximum length (L_c), while t_{ret} shows the time taken by the cavity to retract. This is also the time scale of the condensation shock front propagation if the

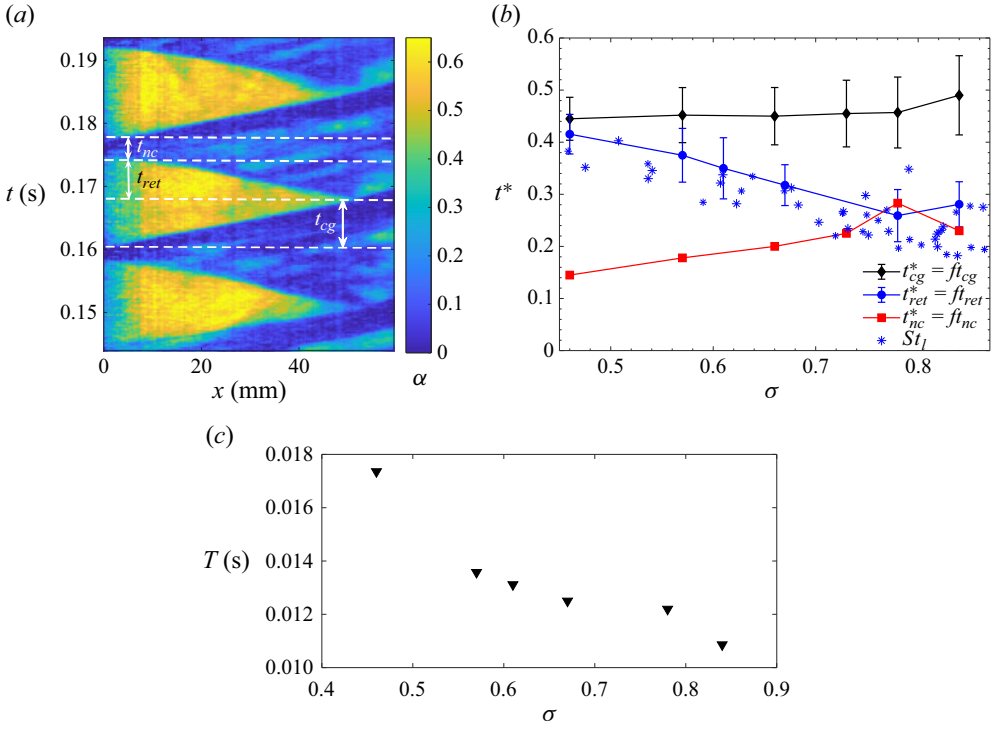

Figure 20. Time scales (t^*) involved in the cavity destabilisation. (a) The x–t diagram for $\sigma = 0.47$ explaining $t \in (t_{cg}, t_{ret}, t_{nc})$. ($b$) Normalised time scales (t^*) at different σ. The star markers show the global cloud shedding frequency expressed as the Strouhal number ($St_l = fL_c/U_t$) measured by Jahangir *et al.* (2018). (c) The shedding time period ($T = 1/f$) as a function of σ.

condensation shock front is responsible for cavity destabilisation and shedding. Further, t_{nc} is the time for which the cavity is completely detached at the venturi throat. All these time scales (t_{cg}, t_{ret}, t_{nc}) are phase-averaged over a number of shedding cycles and normalised with the respective shedding time period (T) to yield the corresponding dimensionless time t^*. Here, T is estimated from the dominant peak in the power spectral density in the FFT of the α signals (see figure 20c). The error bars are attributed to the cycle-to-cycle variations in shedding. It is observed that the cavity for all σ reaches the maximum length (L_c) in about $0.45T$. Consequently, the time scale of cavity destabilisation is constant at $\sim 0.55T$. The time scale of cavity destabilisation includes the cavity detachment time (t^*_{ret}) and no-cavitation time (t^*_{nc}). It is observed that the time scale of the condensation shock front causing cavity detachment (t^*_{ret}) is a strong function of σ, i.e. at lower σ, the shock front requires more time (fraction of a cycle) to retract the cavity completely. Further, this trend agrees well with the variation of the Strouhal number ($St_l = fL_c/U_t$) with σ, reported by Jahangir *et al.* (2018) (see star markers in figure 20b). Hence, the time scale of condensation shock front through the cavity is in agreement with the global shedding frequency. In tandem with this, t_{nc} increases with σ, meaning that the time for which the vapour throat is left cavitation-less increases with σ. This has also been observed in the numerical simulations of cavitating flow over a circular cylinder (Gnanaskandan & Mahesh 2016*b*).

References

van Aarle, W., Palenstijn, W.J., Cant, J., Janssens, E., Bleichrodt, F., Dabravolski, A., De Beenhouwer, J., Joost Batenburg, K. & Sijbers, J. 2016 Fast and flexible X-ray tomography using the ASTRA toolbox. *Opt. Express* **24** (22), 25129.

Aliseda, A. & Heindel, T.J. 2021 X-ray flow visualization in multiphase flows. *Annu. Rev. Fluid Mech.* **53**, 543–567.

Arndt, R.E.A., Song, C.C.S., Kjeldsen, M., He, J. & Keller, A. 2000 Instability of partial cavitation: a numerical/experimental approach. *University of Minnesota Supercomputing Institute Research Report UMSI* 183, pp. 140–155.

Bhatt, A., Ganesh, H. & Ceccio, S.L. 2021 Cavitating flow behind a backward facing step. *Intl J. Multiphase Flow* **139**, 103584.

Bhatt, A., Ganesh, H. & Ceccio, S.L. 2023 Partial cavity shedding on a hydrofoil resulting from re-entrant flow and bubbly shock waves. *J. Fluid Mech.* **957**, 1–36.

Bhatt, M. & Mahesh, K. 2020 Numerical investigation of partial cavitation regimes over a wedge using large eddy simulation. *Intl J. Multiphase Flow* **122**, 103155.

Blake, J.R. & Gibson, D.C. 1987 Cavitation bubbles near boundaries. *Annu. Rev. Fluid Mech.* **19**, 99–123.

Brandao, F.L., Bhatt, M. & Mahesh, K. 2019 Numerical study of cavitation regimes in flow over a circular cylinder. *J. Fluid Mech.* **885**, A19.

Brennen, C.E. 1995 *Cavitation and Bubble Dynamics*. Oxford University Press.

Budich, B., Schmidt, S.J. & Adams, N.A. 2018 Numerical simulation and analysis of condensation shocks in cavitating flow. *J. Fluid Mech.* **838**, 759–813.

Callenaere, M., Franc, J.P., Michel, J.M. & Riondet, M. 2001 The cavitation instability induced by the development of a re-entrant jet. *J. Fluid Mech.* **444**, 223–256.

Coutier-Delgosha, O., Devillers, J.F., Pichon, T., Vabre, A., Woo, R. & Legoupil, S. 2006 Internal structure and dynamics of sheet cavitation. *Phys. Fluids* **18** (1), 017103.

Dash, A., Jahangir, S. & Poelma, C. 2018 Direct comparison of shadowgraphy and X-ray imaging for void fraction determination. *Meas. Sci. Technol.* **29**, 125303.

Ganesh, H., Makiharju, S.A. & Ceccio, S.L. 2016 Bubbly shock propagation as a mechanism for sheet-to-cloud transition of partial cavities. *J. Fluid Mech.* **802**, 37–78.

Gawandalkar, U. & Poelma, C. 2022 The structure of near-wall re-entrant flow and its influence on cloud cavitation instability. *Exp. Fluids* **63** (5), 1–19.

Gnanaskandan, A. & Mahesh, K. 2016*a* Large eddy simulation of the transition from sheet to cloud cavitation over a wedge. *Intl J. Multiphase Flow* **83**, 86–102.

Gnanaskandan, A. & Mahesh, K. 2016*b* Numerical investigation of near-wake characteristics of cavitating flow over a circular cylinder. *J. Fluid Mech.* **790**, 453–491.

Jahangir, S., Hogendoorn, W. & Poelma, C. 2018 Dynamics of partial cavitation in an axisymmetric converging–diverging nozzle. *Intl J. Multiphase Flow* **106**, 34–45.

Jahangir, S., Wagner, E.C., Mudde, R.F. & Poelma, C. 2019 Void fraction measurements in partial cavitation regimes by X-ray computed tomography. *Intl J. Multiphase Flow* **120**, 103085.

Karathanassis, I.K., Heidari-Koochi, M., Zhang, Q., Hwang, J., Koukouvinis, P., Wang, J. & Gavaises, M. 2021 X-ray phase contrast and absorption imaging for the quantification of transient cavitation in high-speed nozzle flows. *Phys. Fluids* **33** (3), 032102.

Kawanami, Y., Kato, H., Yamaguchi, H., Tanimura, M. & Tagaya, Y. 1997 Mechanism and control of cloud cavitation. *Trans. ASME J. Fluids Engng* **119** (4), 788–794.

Knapp, R.T. 1958 Recent investigations of the mechanics of cavitation and cavitation damage. *Wear* **1** (5), 455.

Leroux, J.B., Jacques André, A. & Billard, J.Y. 2004 An experimental study of unsteady partial cavitation. *Trans. ASME J. Fluids Engng* **126** (1), 94–101.

Mäkiharju, S.A., Gabillet, C., Paik, B.G., Chang, N.A., Perlin, M. & Ceccio, S.L. 2013 Time-resolved two-dimensional X-ray densitometry of a two-phase flow downstream of a ventilated cavity. *Exp. Fluids* **54** (7), 1–21.

Mitroglou, N., Lorenzi, M., Santini, M. & Gavaises, M. 2016 Application of X-ray micro-computed tomography on high-speed cavitating diesel fuel flows. *Exp. Fluids* **57** (11), 1–14.

Münch, B., Trtik, P., Marone, F. & Stampanoni, M. 2009 Stripe and ring artifact removal with combined wavelet–Fourier filtering. *Opt. Express* **17**, 8567–8591.

Poelma, C. 2020 Measurement in opaque flows: a review of measurement techniques for dispersed multiphase flows. *Acta Mechanica* **231** (6), 2089–2111.

Prosperetti, A. 2015 The speed of sound in a gas – vapour bubbly liquid. *Interface Focus* **5** (5), 20150024.

REISMAN, G.E., WANG, Y.C. & BRENNEN, C.E. 1998 Observations of shock waves in cloud cavitation. *J. Fluid Mech.* **355**, 255–283.

SHAMSBORHAN, H., COUTIER-DELGOSHA, O., CAIGNAERT, G. & ABDEL NOUR, F. 2010 Experimental determination of the speed of sound in cavitating flows. *Exp. Fluids* **49** (6), 1359–1373.

STUTZ, B. & LEGOUPIL, S. 2003 X-ray measurements within unsteady cavitation. *Exp. Fluids* **35**, 130–138.

TRUMMLER, T., SCHMIDT, S.J. & ADAMS, N.A. 2020 Investigation of condensation shocks and re-entrant jet dynamics in a cavitating nozzle flow by large-eddy simulation. *Intl J. Multiphase Flow* **125**, 103215.

WU, J., DEIJLEN, L., BHATT, A., GANESH, H. & CECCIO, S.L. 2021 Cavitation dynamics and vortex shedding in the wake of a bluff body. *J. Fluid Mech.* **917**, 1–32.

WU, J., GANESH, H. & CECCIO, S. 2019 Multimodal partial cavity shedding on a two-dimensional hydrofoil and its relation to the presence of bubbly shocks. *Exp. Fluids* **60** (4), 1–17.

ZHANG, G., KHLIFA, I., FEZZAA, K., GE, M. & COUTIER-DELGOSHA, O. 2020 Experimental investigation of internal two-phase flow structures and dynamics of quasi-stable sheet cavitation by fast synchrotron X-ray imaging. *Phys. Fluids* **32** (11), 113310.

ZHANG, G., ZHANG, D., GE, M., PETKOVŠEK, M. & COUTIER-DELGOSHA, O. 2022 Experimental investigation of three distinct mechanisms for the transition from sheet to cloud cavitation. *Intl J. Heat Mass Transfer* **197**, 123372.